Supporting Information

Spacer-Cation Electronic Structure Controls Excited-State Pathways in Two-Dimensional Hybrid Perovskites

Camryn J. Gloor,[1] Zijian Gan,[1] Jordan Shanahan,[1] William A. Hearne,[1] Chun-Hsing Chen,[1] Sampreeti Bhattacharya,[1] Jun Hu,[1] Liang Yan,[1] Yosuke Kanai,[1] Andrew M. Moran,[1] Wei You[1*]*

[1]Department of Chemistry, University of North Carolina at Chapel Hill, Chapel Hill, NC 27599-3290 (USA)

Corresponding Authors

*Wei You − Department of Chemistry, University of North Carolina at Chapel Hill, Chapel Hill, North Carolina 27599, United States
Email: wyou@unc.edu

*Andrew M Moran − Department of Chemistry, University of North Carolina at Chapel Hill, Chapel Hill, North Carolina 27599, United States
Email: ammoran@email.unc.edu

Table of Contents

1. Schematic Figures

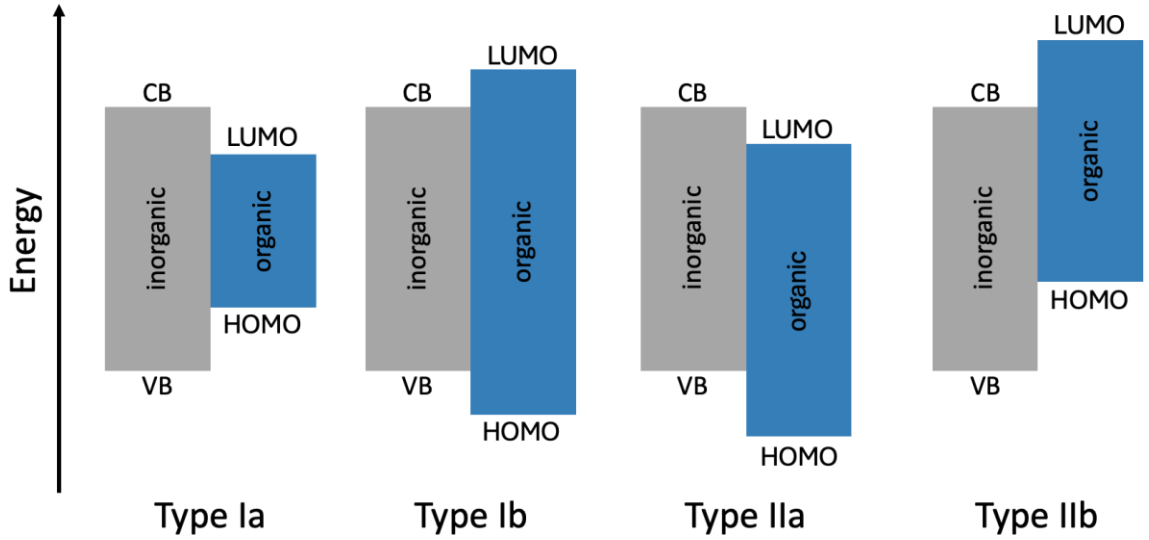

Figure S1 | Possible band alignments between inorganic (gray) energy levels and organic (blue) energy levels in 2D OIHPs.

2. Synthesis of Organic Cations

2.1 Cation Synthesis

All starting materials were purchased from Sigma-Aldrich or TCI Chemical and used without further purification. P-tolunitrile (98% pure) was purchased from Sigma-Aldrich. tert-butyl 4-cyanobenzylcarbamate (95-98% pure) was purchased from Sigma-Aldrich (95-98% pure). 3-amino-propionitrile was purchased from Sigma-Aldrich. 3-Mercaptopropionic Acid (98% pure) was purchased from TCI Chemical. Synthesis was adapted from reference paper.[1]

Scheme S1 | Synthesis Route of MeTzEACl, MePTzEACl, and MeTzPMACl.

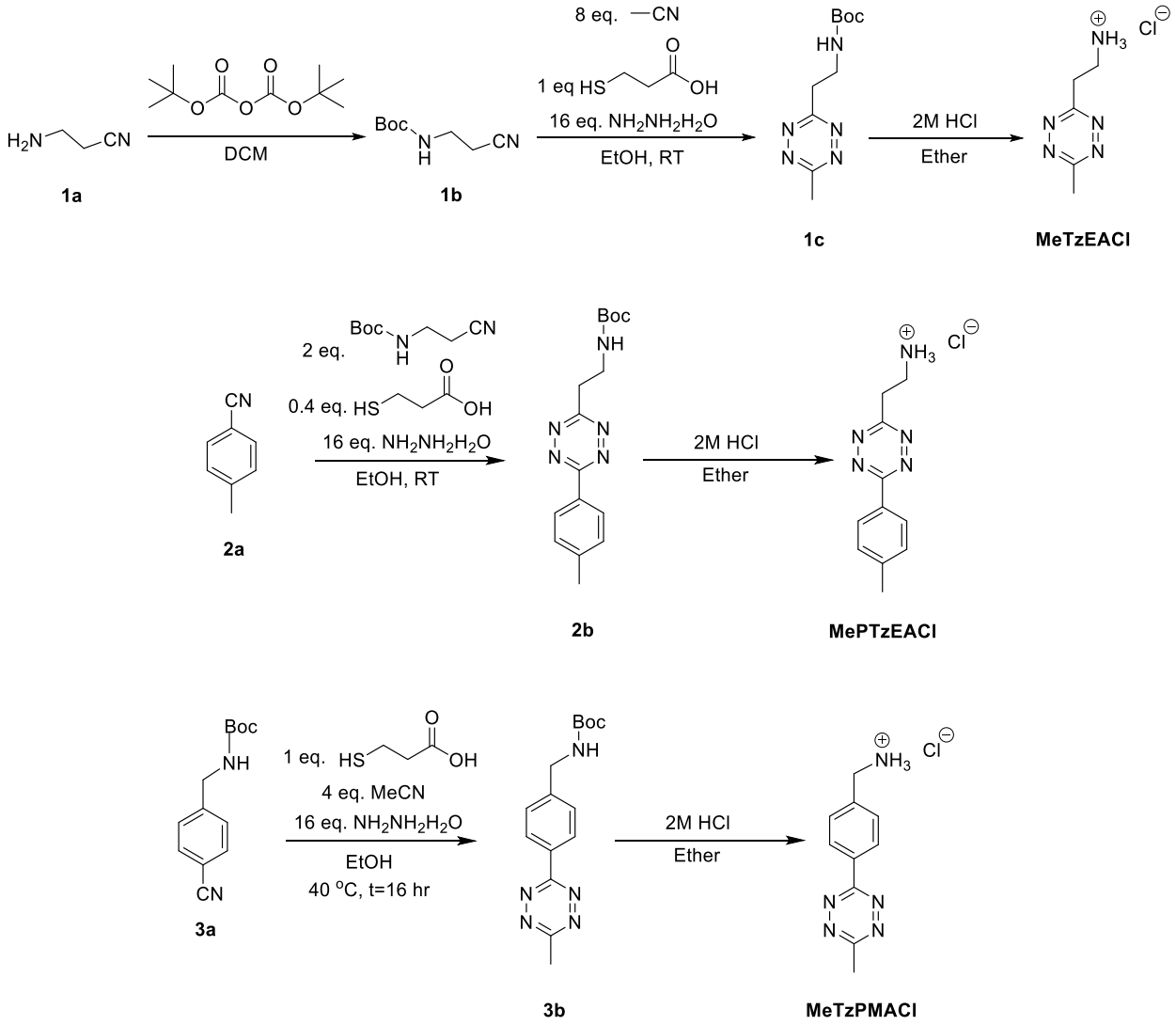

1b 3-aminopropanenitrile (5.00 g, 1 Eq, 71.3 mmol) was added to a 50 mL flask with 30 mL of DCM. di-tert-butyl dicarbonate (20.2 g, 1.3 Eq, 92.7 mmol) was added slowly and gas evolution

was observed at room temperature. The solution was stirred overnight then added to saturated sodium bicarbonate solution to remove excess starting material. The latter solution was extracted with ethyl acetate three times, washed with brine, and dried over magnesium sulfate. The concentrated fraction was used without further purification. ^{1}H NMR (400 MHz, $CDCl_3$) δ 4.97 (s, 1H), 3.39 (q, J = 6.3 Hz, 2H), 2.59 (t, J = 6.3 Hz, 2H), 1.44 (s, 9H).

1c Tert-butyl (2-cyanoethyl)carbamate (4.000 g, 1 Eq, 23.50 mmol), acetonitrile (7.718 g, 9.82 mL, 8 Eq, 188.0 mmol),3-mercaptopropanoic acid (2.494 g, 2.048 mL, 1 Eq, 23.50 mmol), and ethanol (3 mL) were added to a 250 mL round bottom flask and cooled to 0 °C. Afterwards, hydrazine hydrate (18.82 g, 18.29 mL, 16 Eq, 376.0 mmol) was added dropwise to the flask, and the reaction was warmed to 40 °C for 18 hours. The precipitate solution was then transferred to a 1 L flask with DCM, and sodium nitrite (24.32 g, 176.3 mL, 2.0 molar, 15 Eq, 352.5 mmol) was added slowly on ice. Afterwards, 1M HCl was added slowly on ice until the color of the solution turned bright pink and gas evolution ceased. The product was extracted with ethyl acetate three times and dried over magnesium sulfate. Further purification by column chromatography 30:1 DCM:EtAc yielded tert-butyl (2-(6-methyl-1,2,4,5-tetrazin-3-yl)ethyl)carbamate (1.800 g, 7.523 mmol, 32.01 %). ^{1}H NMR (400 MHz, $CDCl_3$) δ 5.01 (s, 1H), 3.73 (q, J = 6.2 Hz, 2H), 3.50 (t, J = 6.2 Hz, 2H), 3.05 (s, 3H), 1.39 (s, 9H).

2b 4-methylbenzonitrile (2.000 g, 1 Eq, 17.07 mmol), tert-butyl (2-cyanoethyl)carbamate **1c** (5.812 g, 2 Eq, 34.14 mmol), 3-mercaptopropanoic acid (1.812 g, 1.488 mL, 1.000 Eq, 17.07 mmol) and ethanol (3 mL) were added to a 250 mL round bottom flask, purged with argon for 15 min and cooled to 0 °C. Afterwards, hydrazine hydrate (13.67 g, 13.67 mL, 16.00 Eq, 273.2 mmol) was added dropwise to the flask and the reaction was warmed to 40 °C for 18 hours. The precipitate solution was then transferred to a 1 L flask with DCM, and sodium nitrite (17.67 g, 128.0 mL, 2.00 molar, 15 Eq, 256.1 mmol) was added slowly on ice. Afterwards, 1M HCl was added slowly on ice until the color of the solution turned dark red and gas evolution ceased. The product was extracted with ethyl acetate three times and dried over magnesium sulfate. Further purification by column chromatography 30:1 DCM:EtAc yielded di-tert-butyl ((1,2,4,5-tetrazine-3,6-diyl)bis(ethane-2,1-diyl))dicarbamate (1.202 g, 3.262 mmol, 19.11 %). ^{1}H NMR (400 MHz, $CDCl_3$) δ 8.49 (d, J = 8.3 Hz, 2H), 7.40 (d, J = 8.0 Hz, 2H), 5.07 (s, 1H), 3.78 (q, J = 6.2 Hz, 2H), 3.55 (dd, J = 6.7, 5.5 Hz, 2H), 2.48 (s, 3H), 1.38 (s, 9H).

3b tert-butyl (4-cyanobenzyl)carbamate (1.328 g, 1 Eq, 5.717 mmol), acetonitrile (1.878 g, 2.39 mL, 8 Eq, 45.74 mmol) 3-mercaptopropanoic acid (606.8 mg, 498.2 µL, 1 Eq, 5.717 mmol) and ethanol (1 mL) were added to a 250 mL round bottom flask, purged with argon for 15 min and cooled to 0 °C. Afterwards, hydrazine hydrate (4.579 g, 4.450 mL, 16 Eq, 91.48 mmol) was added dropwise to the flask, and the reaction was warmed to 40 °C for 16 hours. The precipitate solution was then transferred to a 1 L flask with DCM, and sodium nitrite (5.916 g, 42.88 mL, 2.0 molar, 15 Eq, 85.76 mmol) was added slowly on ice. Afterwards, 1M HCl was added slowly on ice until the color of the solution turned dark red and gas evolution ceased. The product was extracted with ethyl acetate three times and dried over magnesium sulfate. Further purification by column

chromatography 20:1 DCM:EtAc yielded tert-butyl (4-(6-methyl-1,2,4,5-tetrazin-3-yl)benzyl)carbamate (1.072 g, 3.557 mmol, 62.22 %). ^{1}H NMR (400 MHz, $CDCl_3$) δ 8.56 (d, J = 8.4 Hz, 2H), 7.51 (d, J = 8.3 Hz, 2H), 4.96 (s, 1H), 4.44 (d, J = 6.1 Hz, 2H), 3.10 (s, 3H), 1.48 (s, 9H).

General procedure for the synthesis of Ammonium Chloride salts: 1.5 mmol of Boc-protected tetrazine (1c, 2b, or 3b) was added to a 20 mL vial and dissolved in 5 mL of 2M HCl in dry ether with vigorous stirring. Within 3 hours, the complete precipitation of each tetrazine was observed and collected via vacuum filtration, and the solid was washed with excess cold ether to produce a quantitative yield of each salt.

MeTzEACl: ^{1}H NMR (400 MHz, DMSO) δ 7.98 (m, 3H), 3.57 (t, *J* = 7.0 Hz, 2H), 3.40 (m, 2H), 2.98 (s, 3H). ^{13}C NMR (151 MHz, $CDCl_3$) δ 167.74, 166.53, 37.08, 32.21, 21.01.

MePTzEACl: ^{1}H NMR (400 MHz, DMSO) δ 8.40 (d, J = 8.3 Hz, 2H), 7.97 (m, 3H), 7.50 (d, J = 8.2 Hz, 2H), 3.63 (t, J = 6.9 Hz, 2H), 3.45 (m, 2H), 2.45 (s, 3H). ^{13}C NMR (151 MHz, $CDCl_3$) δ 166.71, 163.97, 143.48, 130.53, 129.12, 127.80, 127.77, 37.22, 32.38, 21.45.

MeTzPMACl: ^{1}H NMR (400 MHz, DMSO) δ 8.51 (d, J = 8.0 Hz, 2H), 8.36 (m, 3H), 7.75 (d, J = 8.1 Hz, 2H), 4.18 (s, 2H), 3.02 (s, 3H). ^{13}C NMR (151 MHz, $CDCl_3$) δ 166.64, 162.31, 137.41, 131.29, 129.08, 126.98, 41.30, 20.11.

2.2 Characterization of Cations

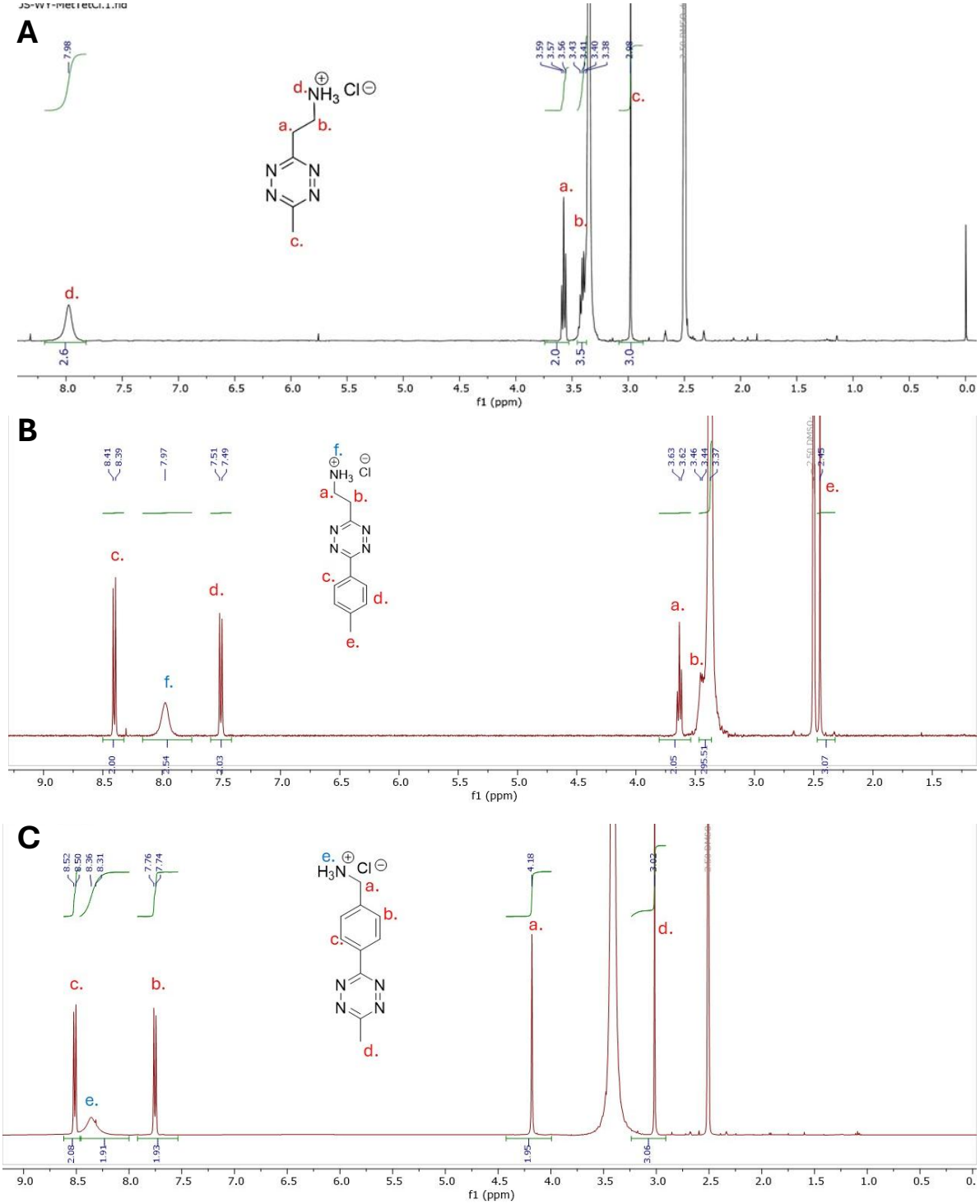

Figure S2 | Structure and ^{1}H NMR of (A) MeTzEACl, (B) MePTzEACl, and (C) MeTzPMACl in DMSO-d6

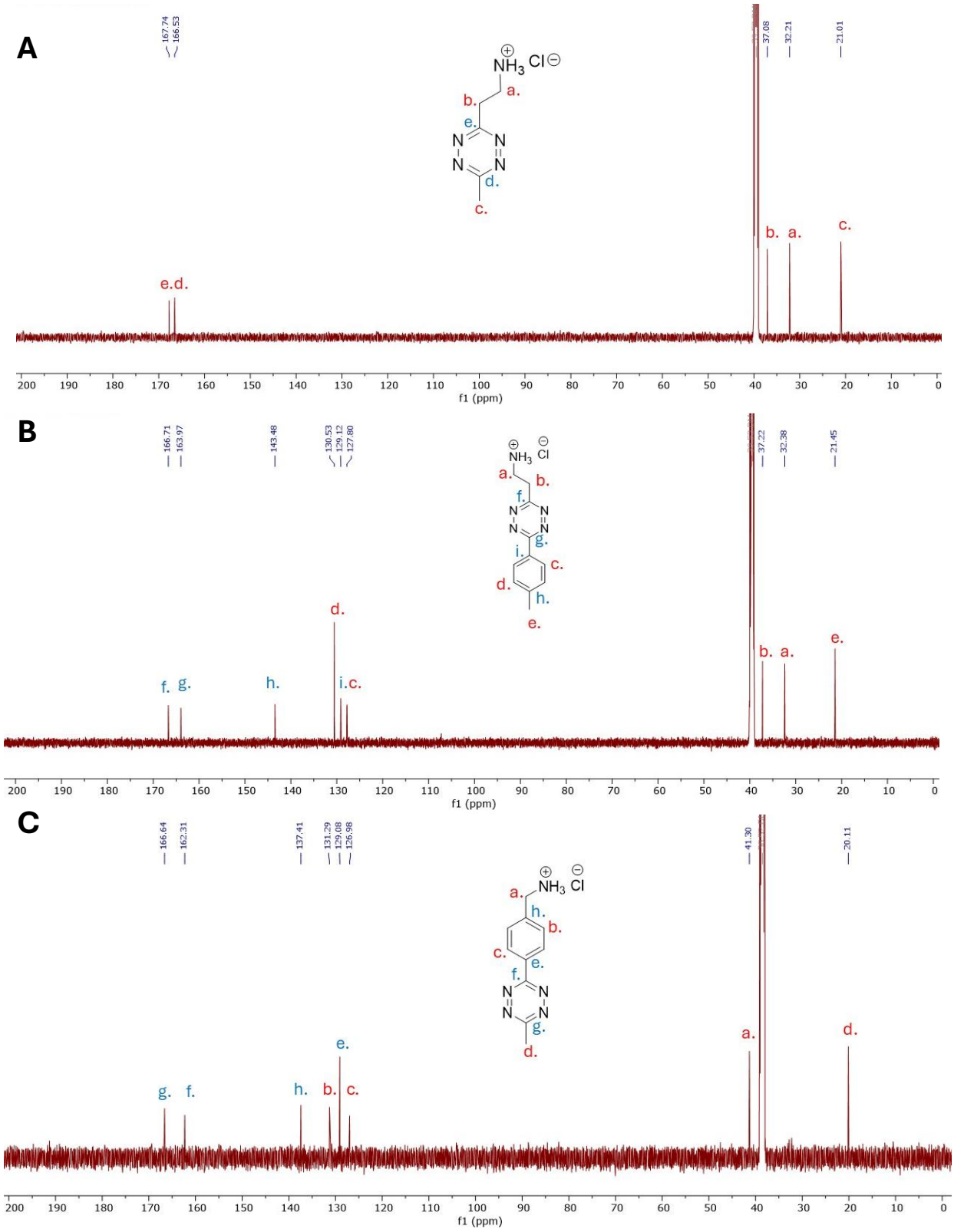

Figure S3 | Structure and ^{13}C NMR of (A) MeTzEACl, (B) MePTzEACl, and (C) MeTzPMACl in DMSO-d6

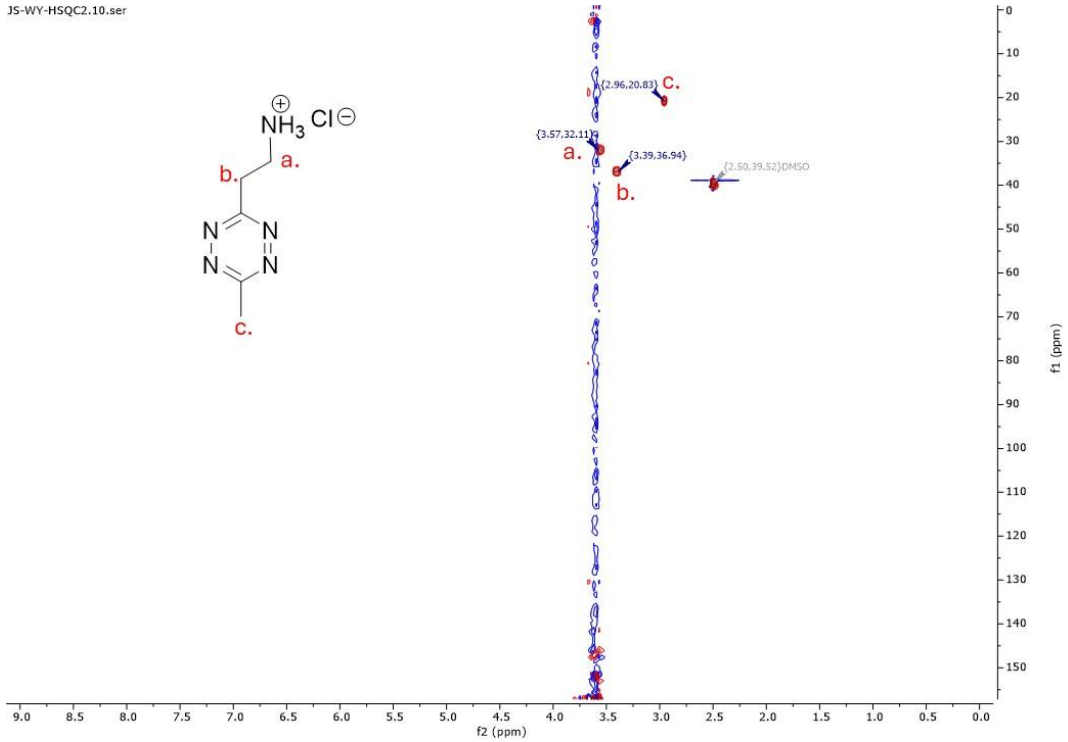

Figure S4 | HSQC 2D-NMR of MeTzEACl in DMSO-d6.

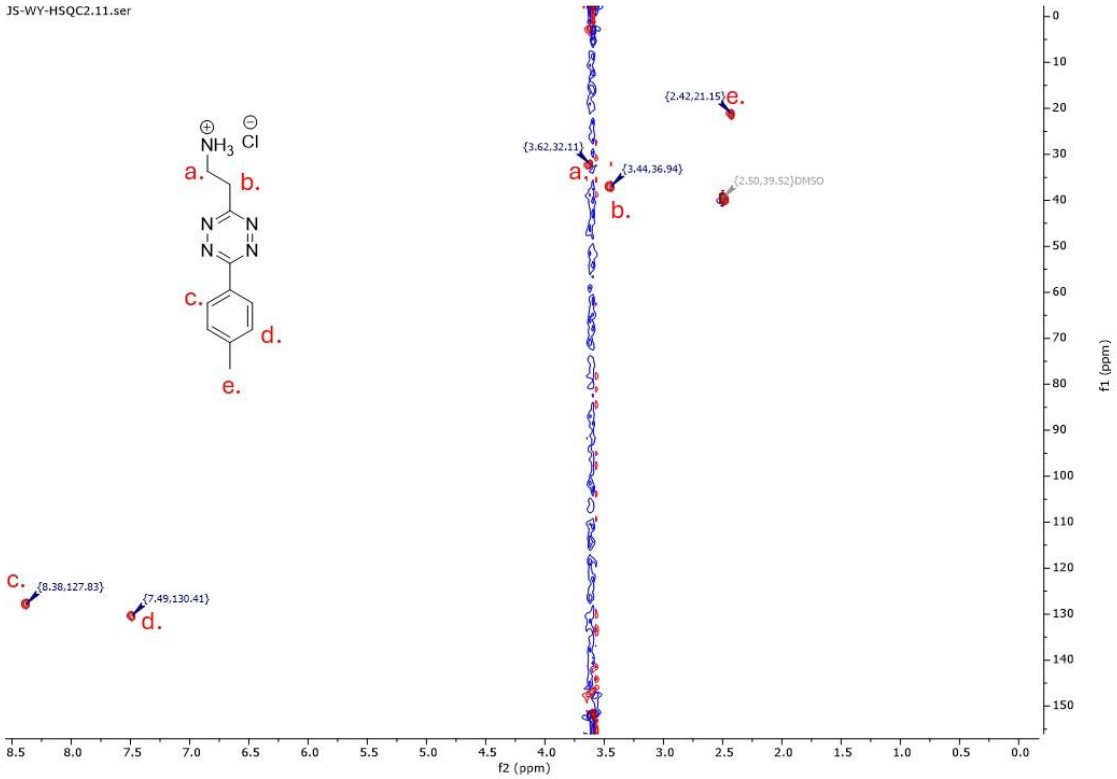

Figure S5 | HSQC 2D-NMR of MePTzEACl in DMSO-d6.

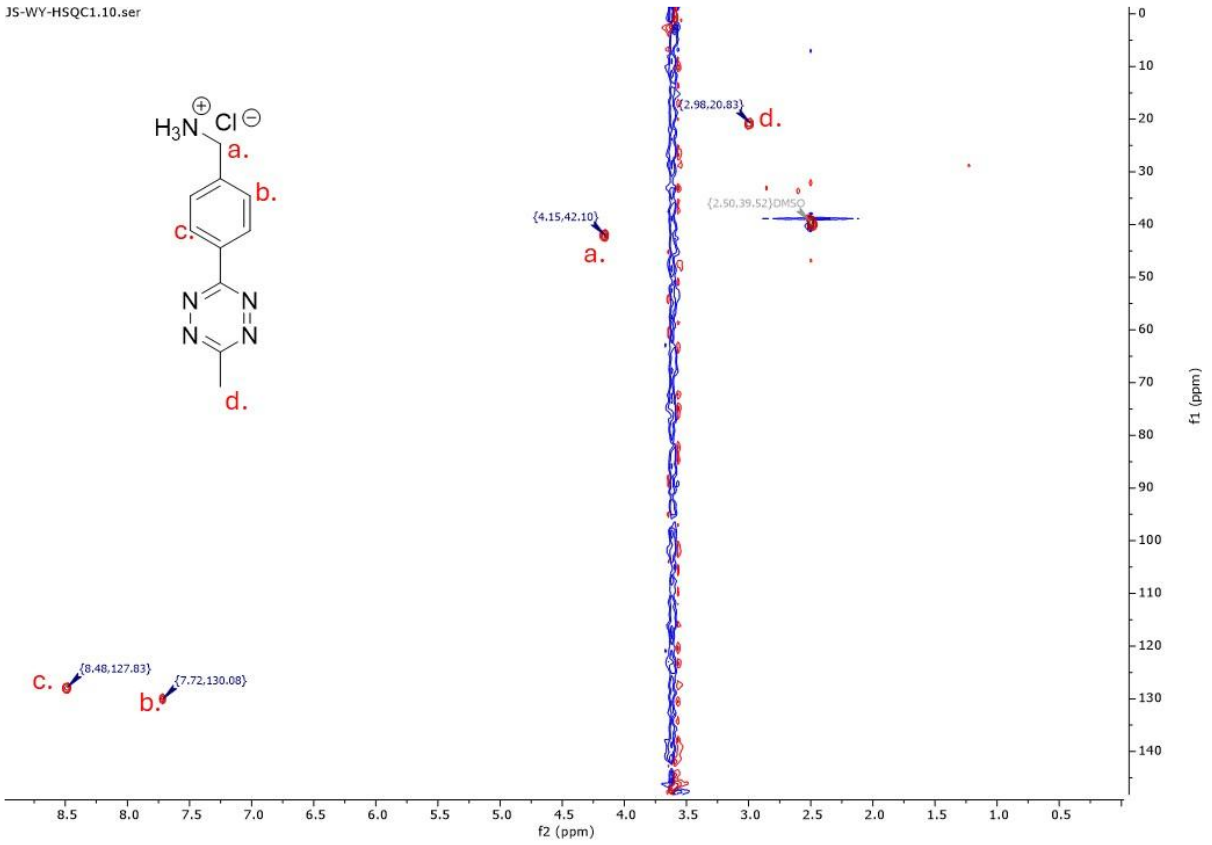

Figure S6 | HSQC 2D-NMR of MeTzPMACl in DMSO-d6.

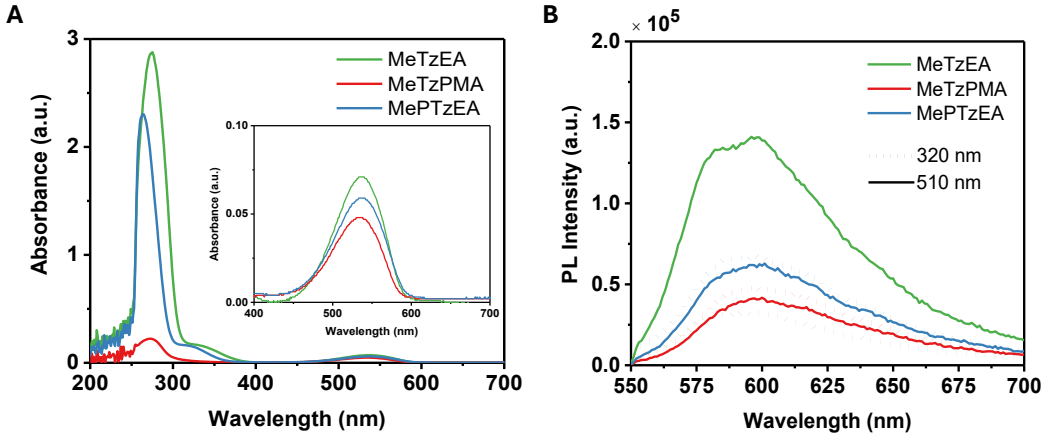

Figure S7 | Optical properties of tetrazine salts. (A) Raw absorbance of tetrazine salts in DMSO. Inset shows the low-energy n-π* transition from 450 nm to 650 nm. (B) Raw photoluminescence (PL) of the tetrazine salts with an excitation wavelength of 320 nm (dotted line) and 510 nm (solid line).

3. Thin Film and Crystal Fabrication

3.1 Materials

All materials were purchased from Sigma-Aldrich ($PbBr_2$, >98%), Fisher ($PbCl_2$, 99.9985%), or Ambeed (BACl, 99.84%) and were used without further purification. Precleaned microscope slides ($25 \times 75 \times 1.0$ mm^3) were purchased from Fisher. Slides were cut to ~$25 \times 25 \times 1.0$ mm^3 and used as substrates to fabricate perovskite films. The glass substrates were further cleaned by sonication in deionized water, acetone, and isopropanol for 15 min each. The substrates were then dried under a stream of nitrogen and treated with UV-Ozone for 15 min.

3.2 Perovskite Thin Films

For BA-based perovskite films, BACl and $PbCl_2$ were dissolved in DMSO with a molar ratio of 2:1 at 0.15 mol/L (Pb^{2+}) concentration. The precursor solution was heated to 100 °C prior to use. The $[BA]_2PbCl_4$ films were then obtained by spin-coating the precursor solution onto a precleaned glass substrate at 3000 rpm for 30 s. After spin coating, the films were immediately annealed at 100 °C for 10 min.

The precursor solutions for MeTzEA and MePTzEA-based films were obtained by dissolving the ammonium salt and $PbCl_2$ in DMSO with a molar ratio of 2:1 at 0.3 mol/L (Pb^{2+}) concentration. The 2D perovskite films were obtained by spin coating the precursor solution onto a precleaned glass substrate at 3000 rpm for 30 s. After spin coating, the films were immediately annealed at 100 °C for 10 min.

For MeTzPMA-based films, the precursor solution was produced by dissolving MeTzPMACl and $PbCl_2$ in DMSO with a molar ratio of 2:1 at 0.2 mol/L (Pb^{2+}) concentration. The 2D perovskite films were obtained by spin coating the precursor solution onto a precleaned glass substrate at 3000 rpm for 30 s. After spin coating, the films were immediately put on top of a hot plate and covered by a glass petri dish. About 10 µL of DMSO was added to the hot plate under the petri dish during the solvent annealing process. Films were annealed at 100 °C for 60 minutes.

To obtain mixed anion perovskite films, chloride-based salts were mixed with $PbBr_2$ at a molar ratio of 2:1. The concentration of Pb^{2+} was 0.15 mol/L for BA-based films and 0.3 mol/L for tetrazine-based films. The $[BA]_2PbBr_2Cl_2$ films were obtained by spin-coating the precursor solution onto a precleaned glass substrate at 3000 rpm for 60 s, followed by thermal annealing at 120 °C for 10 min. The $[MeTzEA]_2PbBr_2Cl_2$ and $[MePTzEA]_2PbBr_2Cl_2$ films were obtained by spin coating the precursor solution onto a precleaned glass substrate at 5000 rpm for 30 s. After spin coating, the films were immediately annealed at 120 °C for 10 min. The $[MeTzPMA]_2PbBr_2Cl_2$ films were obtained by spin coating the precursor solution onto a precleaned glass substrate at 3000 rpm for 30 s. After spin coating, the films were immediately put on top of a hot plate and covered by a glass petri dish. About 10 µL of DMSO was added to the hot plate under the petri dish during the solvent annealing process. Films were annealed at 100 °C

for 60 minutes. The spin-coating process for all systems was conducted in a glovebox filled with N_2 gas.

The use of solvent annealing for MeTzPMA-based films was needed to obtain films with high crystallinity, consistent with previous reports of other 2D OIHPs.[2-4] In contrast, traditional thermal annealing (as applied to our other systems) produced films with pronounced surface roughness and poor crystallinity, evidenced by broadened excitonic absorption features and weak XRD reflections, as shown in **Figure S8**.

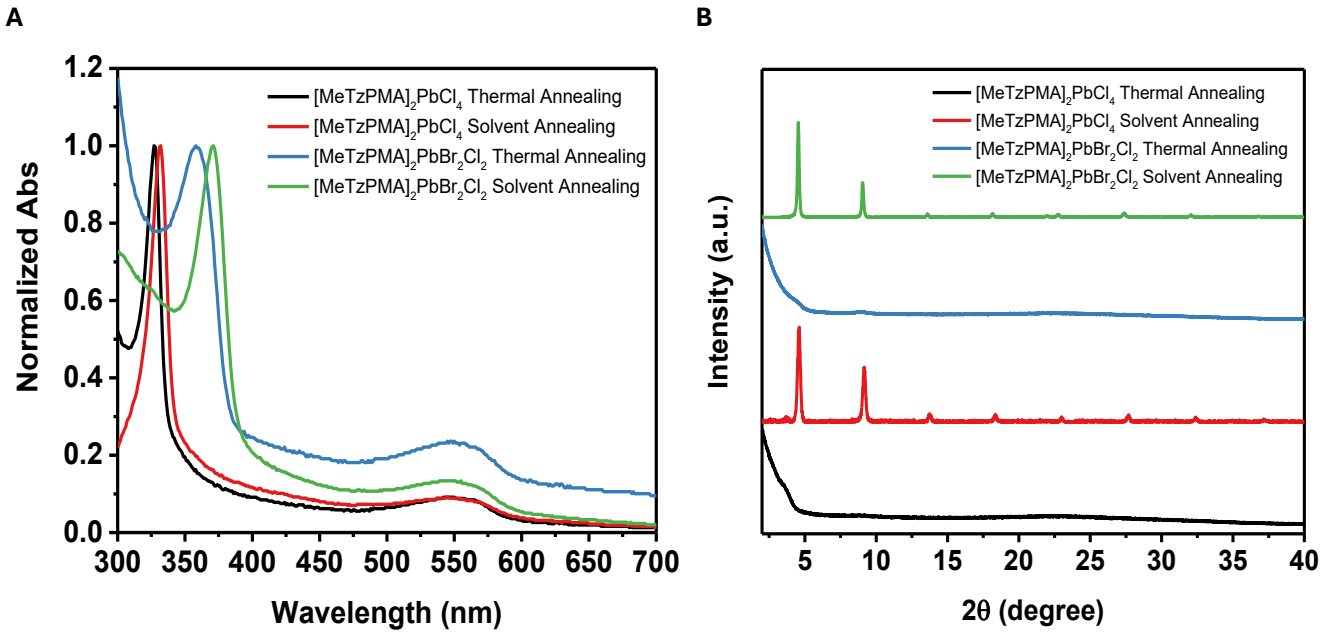

Figure S8 | Comparison of thermal and solvent annealing for MeTzPMA-based perovskite thin films. (A) UV–Vis absorption spectra and (B) XRD patterns of chloride-based films after thermal annealing (black) and solvent annealing (red), and mixed-anion films after thermal annealing (blue) and solvent annealing (green).

3.3 Synthesis of Single Crystal of $[MeTzPMA]_2PbCl_4$

Single crystals were achieved through antisolvent vapor-assisted crystallization (AVC). MeTzPMACl (4.8 mg) and $PbCl_2$ (2.8 mg) were dissolved in 50 uL of DMSO. The solution was then diluted 20 times with DMSO. Then, a 5-mL vial containing 100 uL of solution was placed inside a 20-mL vial containing DCM. The small vial was sealed with PTFE tape, but a small hole was left to let DCM slowly diffuse. After three days, thin pink needle crystals were obtained.

3.4 Synthesis of Single Crystal of $[MePTzEA]_2PbCl_4$

Single crystals were achieved through the AVC method. MePTzEACl (12.6 mg) and $PbCl_2$ (7.0 mg) were dissolved in 250 uL of DMF:DMSO=4:1 to give a precursor solution of 0.1 mol/L Pb^{2+} concentration. A 5-mL vial containing 50 uL of solution was placed inside a 20-mL vial containing chloroform. The small vial was sealed with PTFE tape but left a small hole to let chloroform slowly diffuse. After two days, pink plate-like crystals were obtained.

3.5 Synthesis of Single Crystal of $[MeTzEA]_2PbCl_4$

Single crystals were achieved through the AVC method. MeTzEACl (8.8 mg) and $PbCl_2$ (7.0 mg) were dissolved in 250 uL of DMF:DMSO=1:1 to give a precursor solution of 0.1 mol/L Pb^{2+} concentration. The solution was then diluted 10 times with DMF to achieve 0.01 mol/L Pb^{2+} concentration. A 5-mL vial containing 100 uL of solution was placed inside a 20-mL vial containing chloroform. The small vial was sealed with PTFE tape but left a small hole to let chloroform slowly diffuse. After five days, purple plate-like crystals were obtained.

3.6 Synthesis of Single Crystal of $[BA]_2PbBr_2Cl_2$

Single crystals were achieved through the AVC method. BACl (5.5 mg) and $PbBr_2$ (9.2 mg) were dissolved in 250 uL of DMSO to give a precursor solution of 0.1 mol/L Pb^{2+} concentration. 100 uL of solution was placed inside a 20-mL vial containing chloroform. The small vial was sealed with PTFE tape but left a small hole to let chloroform slowly diffuse. After seven days, colorless crystals were obtained.

3.7 Synthesis of Single Crystal of $[MeTzEA]_2PbBr_2Cl_2$

Single crystals were achieved through the AVC method. MeTzEACl (8.8 mg) and $PbBr_2$ (9.2 mg) were dissolved in 250 uL of DMSO to give a precursor solution of 0.1 mol/L Pb^{2+} concentration. 100 uL of solution was placed inside a 20-mL vial containing chloroform. The small vial was sealed with PTFE tape but left a small hole to let chloroform slowly diffuse. After three days, purple crystals were obtained.

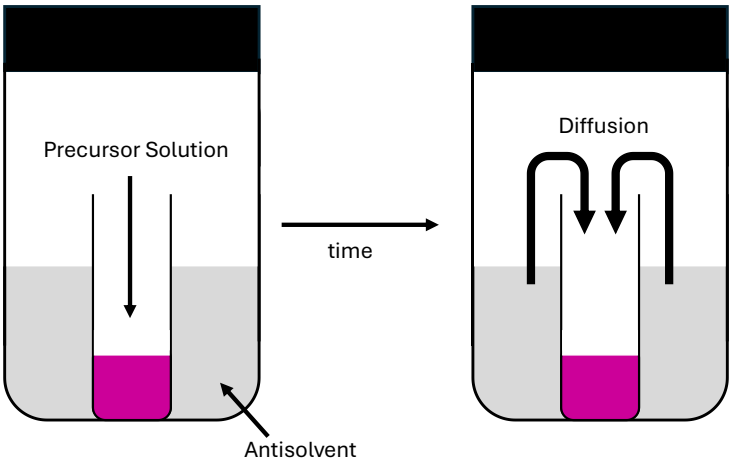

Figure S9 | Schematic of antisolvent vapor-assisted crystallization (AVC) method. A small vial containing precursor solution is placed inside a larger vial containing antisolvent. Over time, the antisolvent will dissolve slowly into the precursor solution.

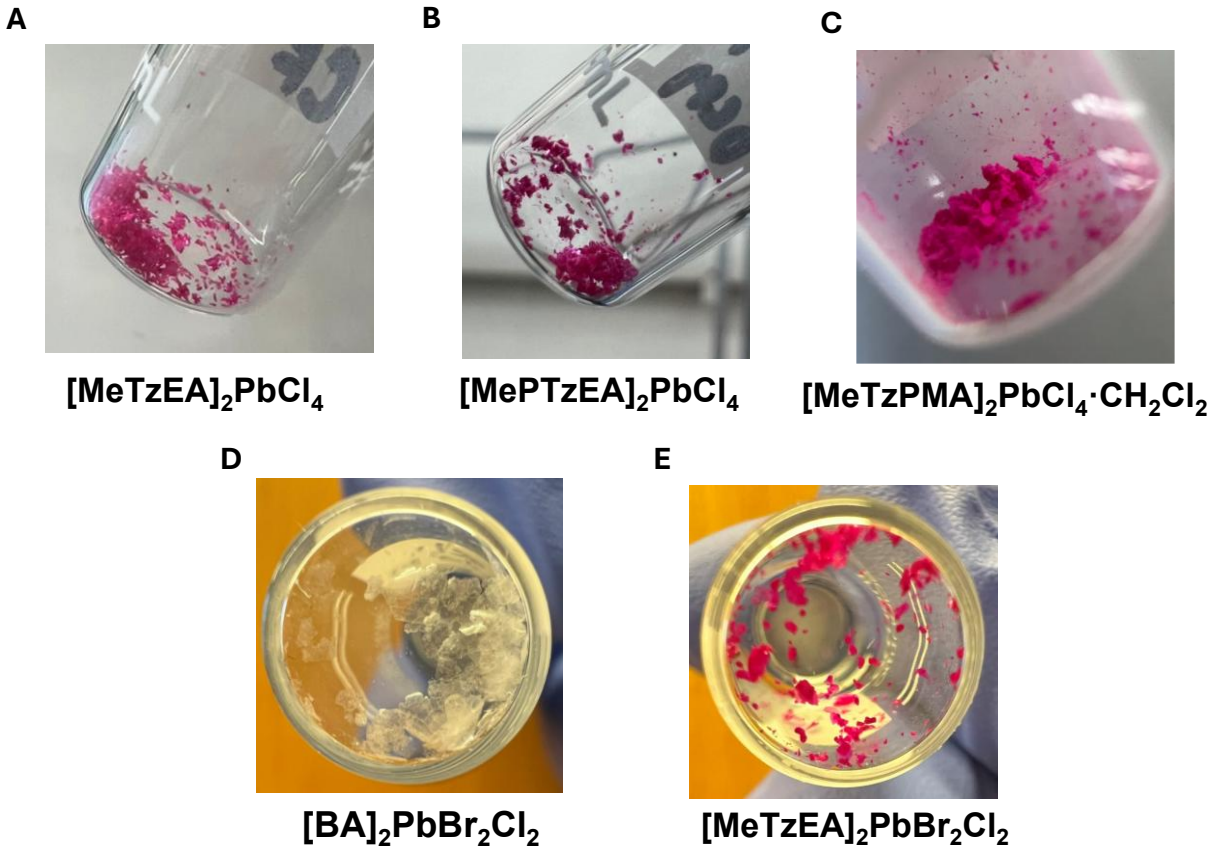

Figure S10 | Photographs of representative single crystals of (A) $[MeTzEA]_2PbCl_4$, (B) $[MePTzEA]_2PbCl_4$, (C) $[MeTzPMA]_2PbCl_4 \cdot CH_2Cl_2$, (D) $[BA]_2PbBr_2Cl_2$, and (E) $[MeTzEA]_2PbBr_2Cl_2$ used for single crystal x-ray diffraction (SCXRD).

4. Perovskite Characterization

4.1 Single Crystal X-Ray Diffraction

Representative data-collection and refinement details for each crystal are summarized below; full crystallographic tables appear in Section 9 (**Tables S2–S6**) and CIF files are provided separately.

$[MeTzPMA]_2PbCl_4$: A pink crystal (approximate dimensions 0.150 x 0.100 x 0.070 mm^3) was placed onto the tip of MiTeGen and mounted on a Bruker D8 VENTURE diffractometer and measured at 150 K. A preliminary set of cell constants was calculated from reflections harvested from a set of 180 frames. These initial sets of frames were oriented such half a sphere in the reciprocal space was surveyed. This produced initial orientation matrices determined from 622 reflections. The data collection was carried out using Cu Kα radiation (graphite monochromator) with theta-dependent frame window of 10-120 seconds and a detector distance of 4.0 cm. A randomly oriented region of reciprocal space was surveyed to achieve complete data with a redundancy of 4. Sections of frames were collected with 2.0º steps in w and f scans. Data to a resolution of 0.84 Å were considered in the reduction. Final cell constants were calculated from the xyz centroids of 4619 strong reflections from the actual data collection after integration (SAINT).[5] The intensity data were corrected for absorption (SADABS).[6] The space group $Pca2_1$ was determined based on intensity statistics and systematic absences. The structure was solved using SHELXT[7] and refined (full-matrix-least squares) using the Oxford University Crystals for Windows system.[8] The dual-space solution provided most non-hydrogen atoms from the E-map. Full-matrix least squares / difference Fourier cycles were performed, which located the remaining non-hydrogen atoms. This structure contains solvent dichloromethane in the organic layer. All non-hydrogen atoms were refined with anisotropic displacement parameters. The hydrogen atoms were placed in ideal positions and refined as riding atoms. The final full matrix least squares refinement converged to R1 = 0.0866 and wR2 = 0.2679 (F^2, all data).

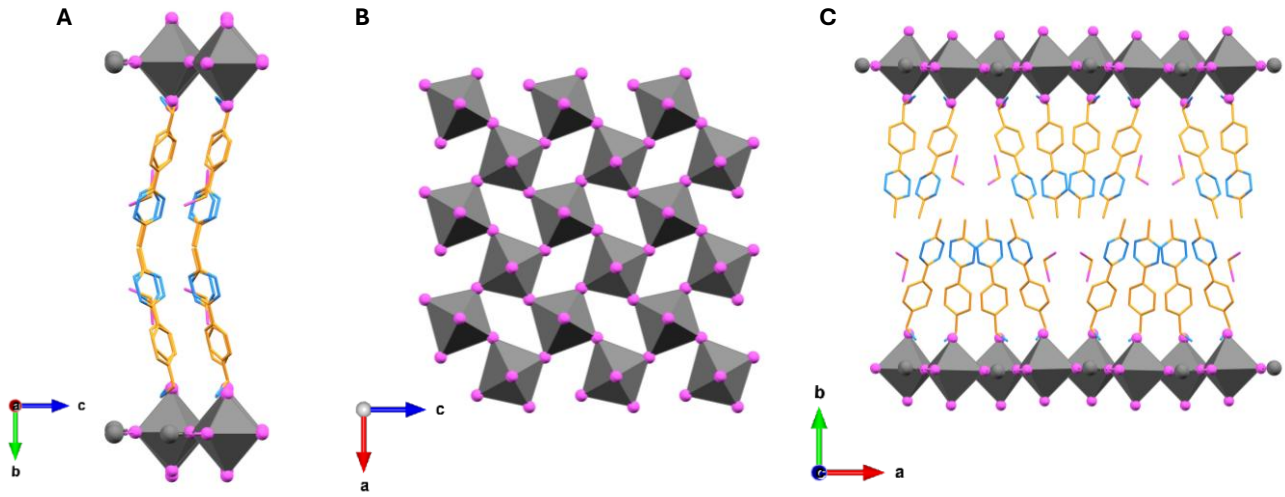

Figure S11 | $[MeTzPMA]_2PbCl_4 \cdot CH_2Cl_2$ crystal structure viewed down various axes. (A) Viewed down *a*-axis, (B) *b*-axis, and (C) *c*-axis. Hydrogens are omitted for clarity. Cl, magenta; C, orange; N, blue; gray diamonds within inorganic layers represent octahedral $[PbCl_6]^{4-}$. Note the presence of residual solvent (dichloromethane).

$[MePTzEA]_2PbCl_4$: A pink crystal (approximate dimensions 0.100 x 0.050 x 0.005 mm^3) was placed onto the tip of MiTeGen and mounted on a Bruker D8 VENTURE diffractometer and measured at 150 K. A preliminary set of cell constants was calculated from reflections harvested from a set of 180 frames. These initial sets of frames were oriented such half a sphere in the reciprocal space was surveyed. This produced initial orientation matrices determined from 622 reflections. The data collection was carried out using Mo Ka radiation (graphite monochromator) with a frame time of 2.5 seconds and a detector distance of 3.7 cm. A randomly oriented region of reciprocal space was surveyed to achieve complete data with a redundancy of 4.7. Sections of frames were collected with 0.60º steps in w and f scans. Data to a resolution of 0.84 Å were considered in the reduction. Final cell constants were calculated from the xyz centroids of 912 strong reflections from the actual data collection after integration (SAINT).[5] The intensity data were corrected for absorption (SADABS).[6] The space group C 1 c 1 was determined based on intensity statistics and systematic absences. The structure was solved using SHELXT[7] and refined (full-matrix-least squares) using the Oxford University Crystals for Windows system.[8] The intrinsic phasing solution provided most non-hydrogen atoms from the E-map. Full-matrix least squares / difference Fourier cycles were performed, which located the remaining non-hydrogen atoms. All non-hydrogen atoms were refined with anisotropic displacement parameters. The hydrogen atoms were placed in ideal positions and refined as riding atoms. The final full matrix least squares refinement converged to R1 = 0.0781 and wR2 = 0.1980 (F^2, all data).

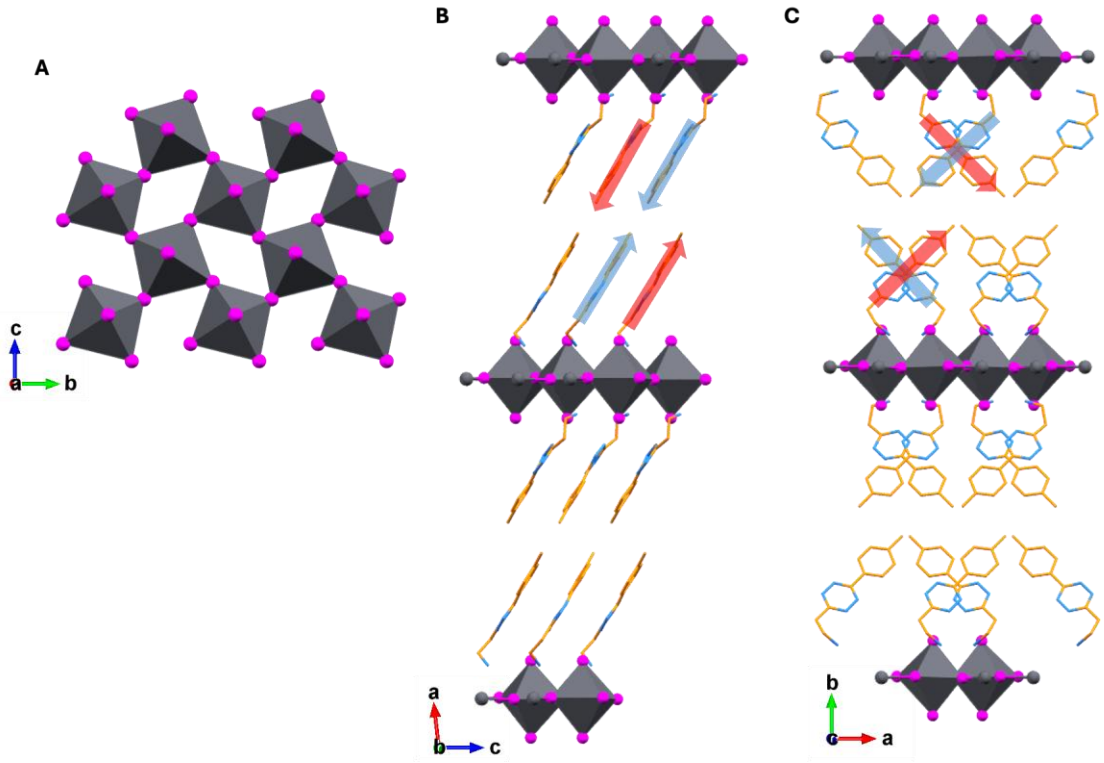

Figure S12 | $[MePTzEA]_2PbCl_4$ crystal structure viewed down various axes. (A) Viewed down *a*-axis, (B) *b*-axis, and (C) *c*-axis. Hydrogens are omitted for clarity. Cl, magenta; C, orange; N, blue; gray diamonds within inorganic layers represent octahedral $[PbCl_6]^{4-}$. Red arrows indicate organic cation going into the plane of the page, while blue arrows indicate going away from the plane of the page.

$[MeTzEA]_2PbCl_4$: A purple crystal (approximate dimensions 0.080 x 0.080 x 0.005 mm^3) was placed onto the tip of MiTeGen and mounted on a Bruker D8 VENTURE diffractometer and measured at 150 K. A preliminary set of cell constants was calculated from reflections harvested from a set of 180 frames. These initial sets of frames were oriented such half a sphere in the reciprocal space was surveyed. This produced initial orientation matrices determined from 630 reflections. The data collection was carried out using Mo Ka radiation (graphite monochromator) with a theta dependent frame time of 10-15 seconds and a detector distance of 3.7 cm. A randomly oriented region of reciprocal space was surveyed to achieve complete data with a redundancy of 5.7. Sections of frames were collected with 1.4° steps in w and f scans. Data to a resolution of 0.84 were considered in the reduction. Final cell constants were calculated from the xyz centroids of 5264 strong reflections from the actual data collection after integration (SAINT).[5] The intensity data were corrected for absorption (SADABS).[6] The space group C2/m was determined based on intensity statistics and systematic absences. The structure was solved using Superflip[9] and refined (full-matrix-least squares) using the Oxford University Crystals for Windows system.[8] The charge-

flipping solution provided most non-hydrogen atoms from the E-map. Full-matrix least squares / difference Fourier cycles were performed, which located the remaining non-hydrogen atoms. All non-hydrogen atoms were refined with anisotropic displacement parameters. The hydrogen atoms were placed in ideal positions and refined as riding atoms. The final full matrix least squares refinement converged to R1 = 0.0431 and wR2 = 0.1125 (F^2, all data).

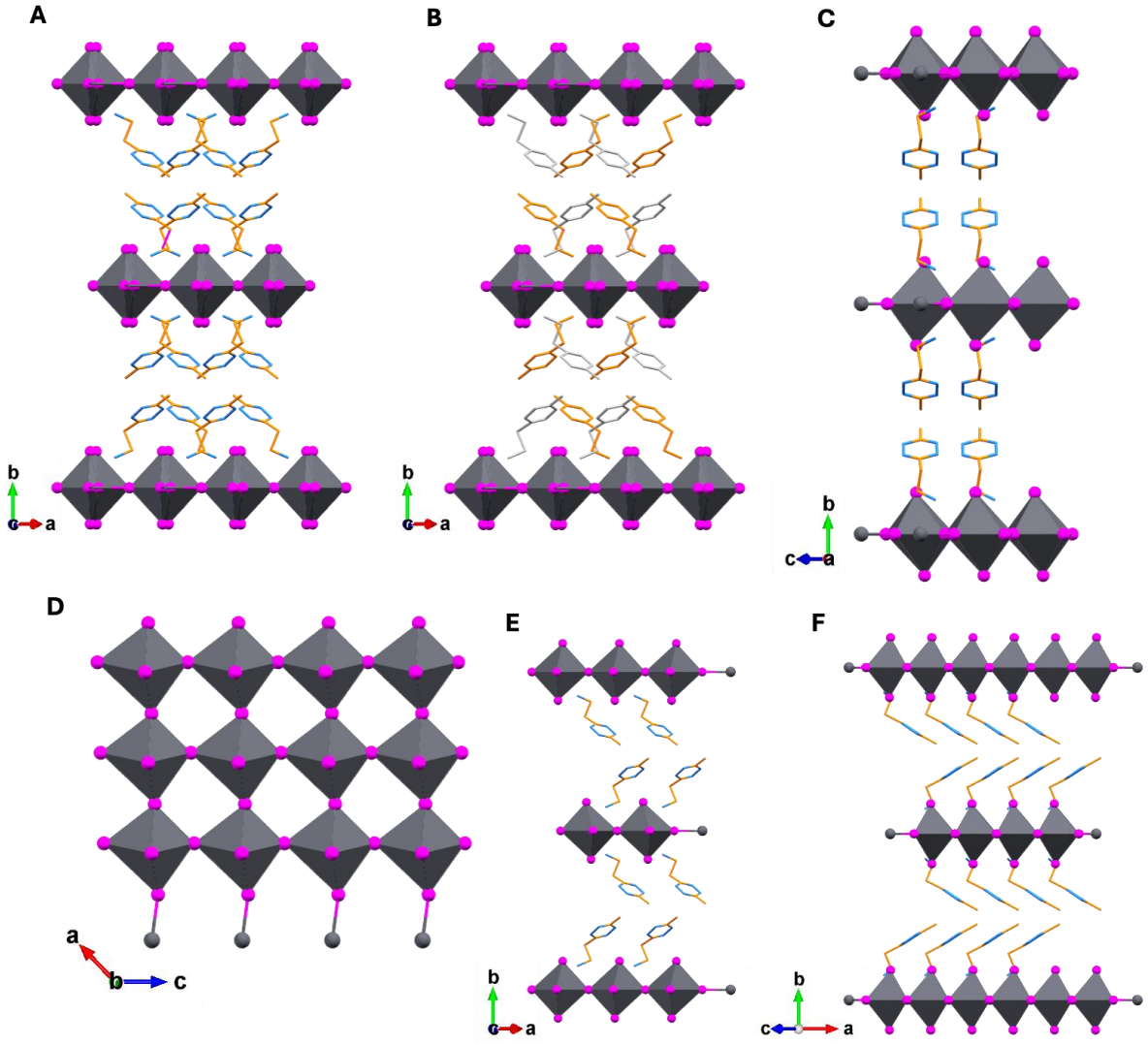

Figure S13 | $[MeTzEA]_2PbCl_4$ crystal structure viewed down various axes. (A) Crystal structure depicting disorder within structure in both the organic and inorganic components. (B) Two possible orientations of organic cations shown in orange and gray. The gray configuration is expanded and viewed down the (C) *a*-axis, (D) *b*-axis, (E) *c*-axis, and (F) *c**-axis. Hydrogens are omitted for clarity. Cl, magenta; C, orange; N, blue; gray diamonds within inorganic layers represent octahedral $[PbCl_6]^{4-}$. In $[MeTzEA]_2PbCl_4$ there is full molecule disorder in both the inorganic and organic layers. The two-part disorder in the lead chloride layer was modeled such that the

occupancies of the major and minor components summed to 1. The tetrazine disorder lies on the 2-fold rotation axis, so the two disorder components were assigned occupancies of 0.5 each.

$[BA]_2PbBr_2Cl_2$: A colorless crystal (approximate dimensions 0.040 x 0.040 x 0.005 mm3) was placed onto the tip of MiTeGen and mounted on a Bruker D8 VENTURE diffractometer and measured at 100 K. A preliminary set of cell constants was calculated from reflections harvested from a set of 180 frames. These initial sets of frames were oriented such half a sphere in the reciprocal space was surveyed. This produced initial orientation matrices determined from 654 reflections. The data collection was carried out using Mo Kα radiation (graphite monochromator) with a frame time of 80 seconds and a detector distance of 4.0 cm. A randomly oriented region of reciprocal space was surveyed to achieve complete data with a redundancy of 4.3. Sections of frames were collected with 1.0° steps in ω and φ scans. Data to a resolution of 0.60 Å were considered in the reduction. Final cell constants were calculated from the xyz centroids of 9922 strong reflections from the actual data collection after integration (SAINT).[5] The intensity data were corrected for absorption (SADABS).[6] The space group I4/m was determined based on intensity statistics and systematic absences. The structure was solved using SHELXT[7] and refined (full-matrix-least squares) using the Oxford University Crystals for Windows system.[8] The intrinsic phasing solution provided most non-hydrogen atoms from the E-map. Full-matrix least squares / difference Fourier cycles were performed, which located the remaining non-hydrogen atoms. All non-hydrogen atoms were refined with anisotropic displacement parameters. The hydrogen atoms were placed in ideal positions and refined as riding atoms. The final full matrix least squares refinement converged to R1 = 0.0756 and wR2 = 0.1863 (F2, all data).

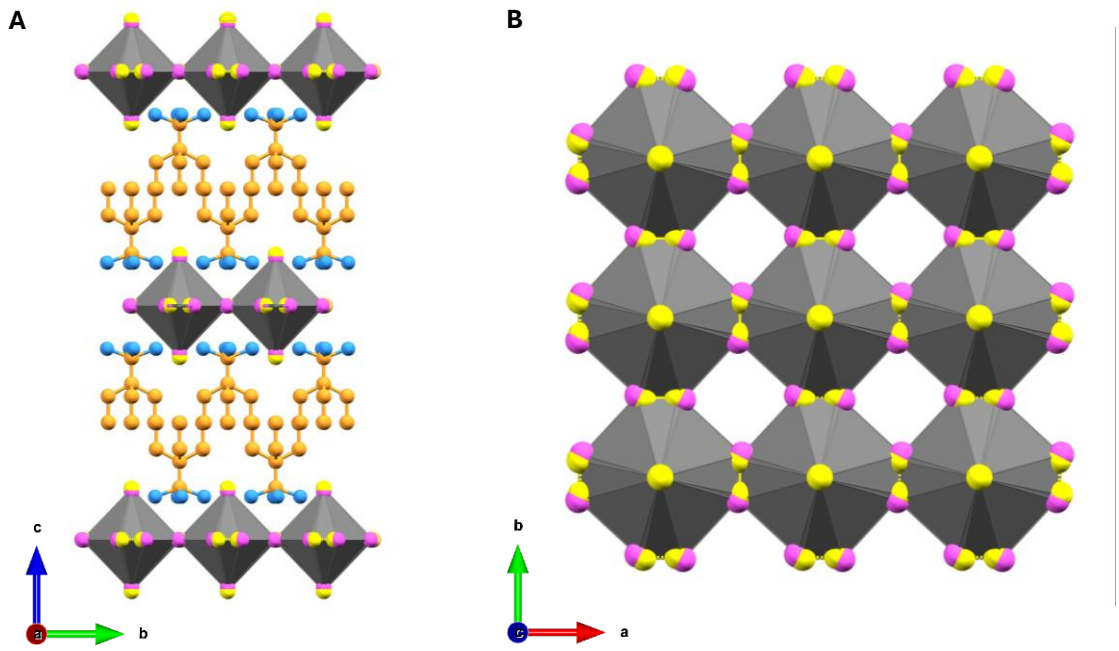

Figure S14 | $[BA]_2PbBr_2Cl_2$ crystal structure, showing all possible orientations of the butylammonium cation, viewed down various axes. (A) Viewed down *a*-axis and (B) *c*-axis. Owing to the four-fold symmetry, all side views appear similar. Significant disorder is present in the inorganic framework, with a 50:50 Cl/Br occupancy at each halide site. Hydrogen atoms are omitted for clarity. Cl, magenta; Br, yellow; C, orange; N, blue; gray diamonds within inorganic layers represent octahedral $[PbBr_3Cl_3]^{4-}$.

$[MeTzEA]_2PbBr_2Cl_2$: A purple crystal (approximate dimensions 0.080 x 0.060 x 0.005 mm3) was placed onto the tip of MiTeGen and mounted on a Bruker D8 VENTURE diffractometer and measured at 150 K. A preliminary set of cell constants was calculated from reflections harvested from a set of 180 frames. These initial sets of frames were oriented such half a sphere in the reciprocal space was surveyed. This produced initial orientation matrices determined from 580 reflections. The data collection was carried out using Mo Ka radiation (graphite monochromator) with a frame time of 100 seconds and a detector distance of 4.0 cm. A randomly oriented region of reciprocal space was surveyed to achieve complete data with a redundancy of 4.7. Sections of frames were collected with 1.50 steps in ω and φ scans. Data to a resolution of 0.70 Å were considered in the reduction. Final cell constants were calculated from the xyz centroids of 8837 strong reflections from the actual data collection after integration (SAINT).[5] The intensity data were corrected for absorption (SADABS).[6] The space group I-4 was determined based on intensity statistics and systematic absences. The structure was solved using SHELXT[7] and refined (full-matrix-least squares) using the Oxford University Crystals for Windows system.[7] The intrinsic phasing solution provided most non-hydrogen atoms from the E-map. Full-matrix least squares / difference Fourier cycles were performed, which located the remaining non-hydrogen atoms. All

non-hydrogen atoms were refined with anisotropic displacement parameters. The hydrogen atoms were placed in ideal positions and refined as riding atoms. The final full matrix least squares refinement converged to R1 = 0.0659 and wR2 = 0.1837 (F2, all data).

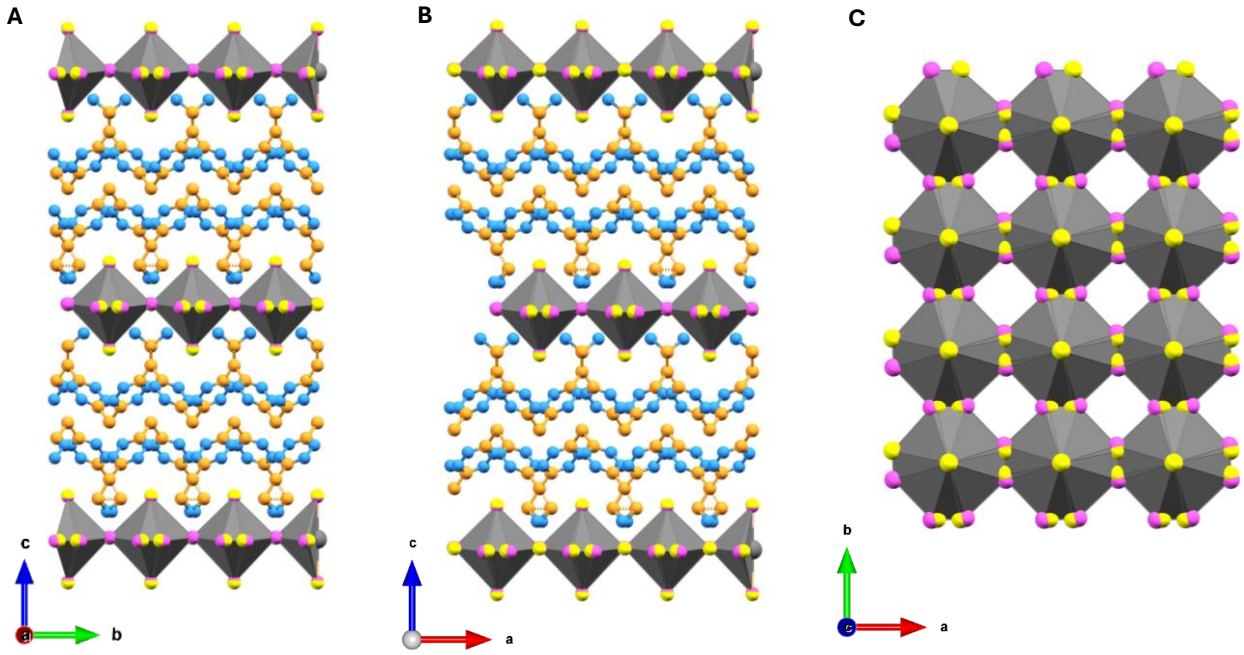

Figure S15 | $[MeTzEA]_2PbBr_2Cl_2$ crystal structure, showing all possible orientations of the tetrazine cation, viewed down various axes. (A) Viewed down *a*-axis, (B) *b*-axis, and (C) *c*-axis. Significant disorder is present in the inorganic framework, with a 50:50 Cl/Br occupancy at each halide site. Hydrogen atoms are omitted for clarity. Cl, magenta; Br; yellow; C, orange; N, blue; gray diamonds within inorganic layers represent octahedral $[PbBr_3Cl_3]^{4-}$.

4.3 Characterization of Thin Films

Thin Film X-Ray Diffraction

Powder X-Ray Diffraction (PXRD) thin film measurements were performed on intact, oriented layered perovskite films using a Rigaku SmartLab X-Ray Diffractometer in the parallel-beam geometry, equipped with a Cu source. All XRD measurements were recorded at room temperature under ambient conditions.

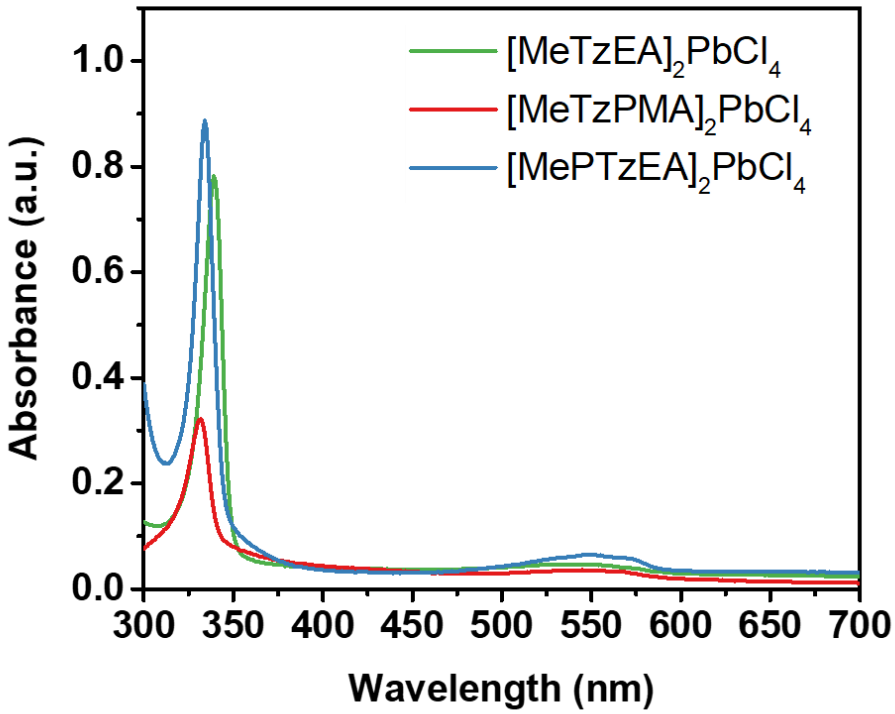

Figure S16 | Raw UV-Vis data of $[MeTzEA]_2PbCl_4$ (green), $[MeTzPMA]_2PbCl_4$ (red), and $[MePTzEA]_2PbCl_4$ (blue) thin films.

X-Ray Photoelectron Spectroscopy

X-Ray photoelectron spectroscopy (XPS) measurements were conducted on mixed anion thin films on glass substrates. X-ray photoelectron spectroscopy (XPS) data was collected on a Kratos Supra+ system with a monochromatic Kα x-ray source operated at 150 W. Survey spectra and high-resolution core-level spectra were acquired, and Ar^+ sputtering was performed to probe near-surface composition. A charge neutralizer was used to prevent charging when necessary and all spectra were corrected to the C 1s peak at 284.6 eV. Kratos ESCApe software was used for data analysis, Shirley baselines were used, and the relative sensitivity factors used for quantification were those from the ESCApe software.

XPS survey spectra were collected over an extended binding energy range to confirm the presence of expected elements; the spectra shown here focus on the core-level regions relevant to halide and lead composition. Atomic percentages of Br and Cl were determined from sensitivity-factor corrected peak areas of the Cl 2p and Br 3d regions.

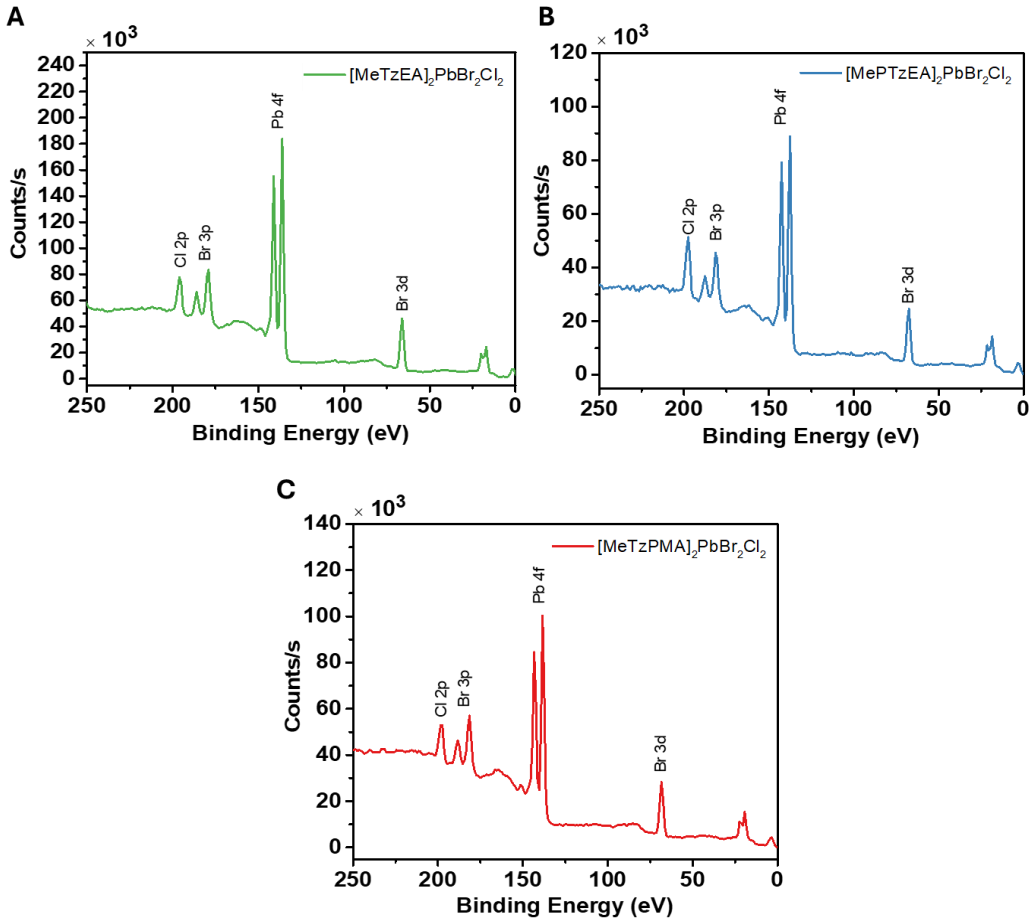

Figure S17 | Representative XPS spectra of (A) $[MeTzEA]_2PbBr_2Cl_2$, (B) $[MePTzEA]_2PbBr_2Cl_2$, and (C) $[MeTzPMA]_2PbBr_2Cl_2$ thin films highlighting the Cl 2p, Br 3d, and Pb 4f core-level peaks. Quantitative Br:Cl ratios obtained from sensitivity-factor corrected peak areas are summarized in **Table S1**.

Table S1 | Br and Cl atomic percentages for mixed-halide perovskite thin films as a function of sputtering depth determined by XPS.

Sample	Film[a]	Etch[b]	Br (at%)	Cl (at%)
$[MeTzEA]_2PbBr_2Cl_2$	1	0	52.8	47.2
		1	53.6	46.4
		2	54.5	45.5
	2	0	52.6	47.4
		1	52.0	48.0
		2	54.2	45.8
$[MePTzEA]_2PbBr_2Cl_2$	1	0	46.1	53.9
		1	50.7	49.3
		2	53.2	46.8
	2	0	46.5	53.5
		1	51.0	49.0
		2	49.1	50.9
$[MeTzPMA]_2PbBr_2Cl_2$	1	0	55.9	44.1
		1	54.6	45.4
		2	54.4	45.6
	2	0	54.0	46.0
		1	56.0	44.0
		2	58.6	41.4

[a] Film 1 and Film 2 correspond to independently prepared samples
[b] Etch number indicates the number of Ar^+ sputtering cycles

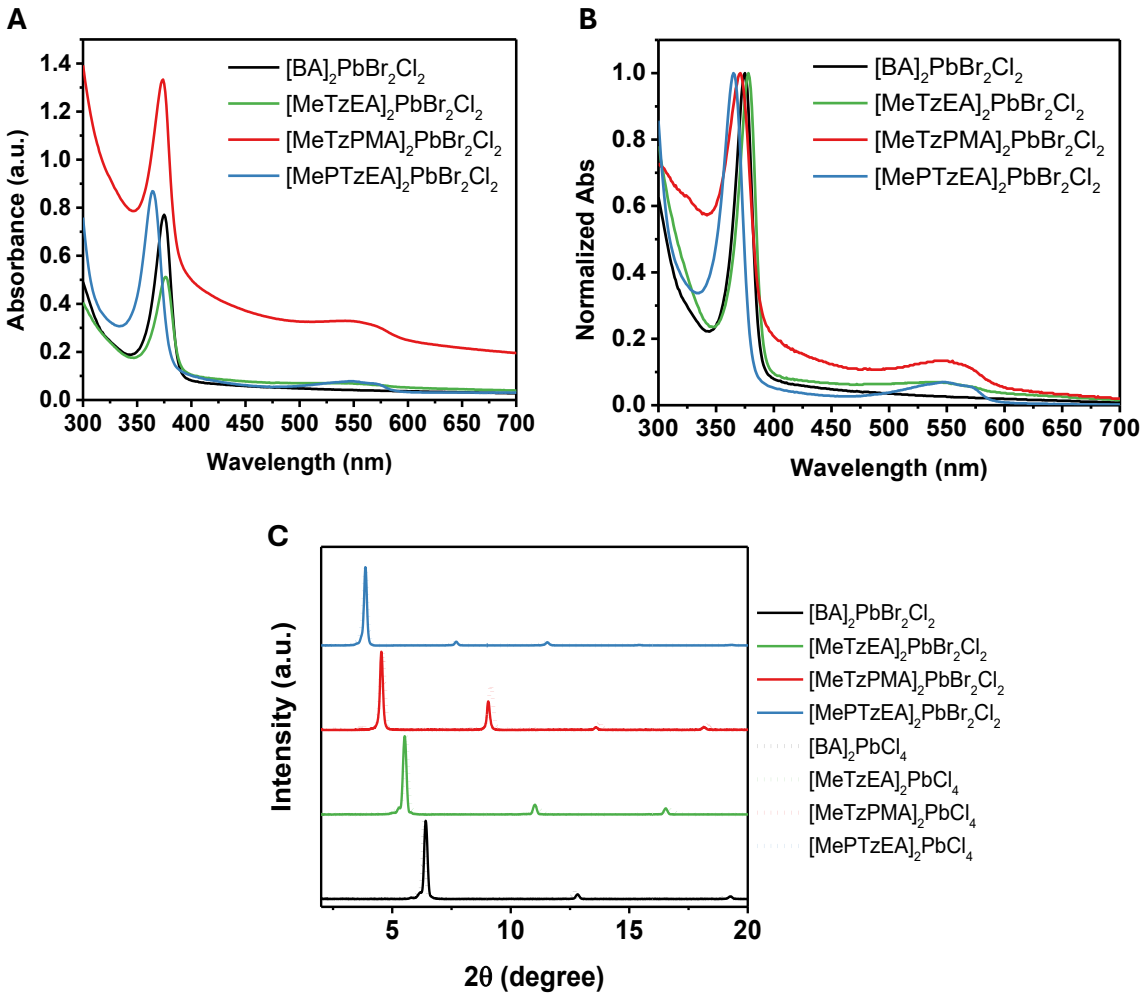

Figure S18 | Characterization of mixed anion films with $[BA]_2PbBr_2Cl_2$ as control. (A) Normalized UV-Vis (B) raw UV-Vis, and (C) comparison of mixed anion films (solid lines) and fully chloride films (dotted lines) powder XRD pattern Notably, the d-spacing, and thus distance between quantum wells, remains consistent with the shift in anion composition.

Scanning Electron Microscopy

Scanning electron microscopy (SEM) images were collected using a Zeiss SUPRA 25 field-emission scanning electron microscope at an accelerating voltage of 2.0 kV. Multiple magnifications (10k and 50k) were imaged. Films were imaged as prepared on glass substrates without additional coating.

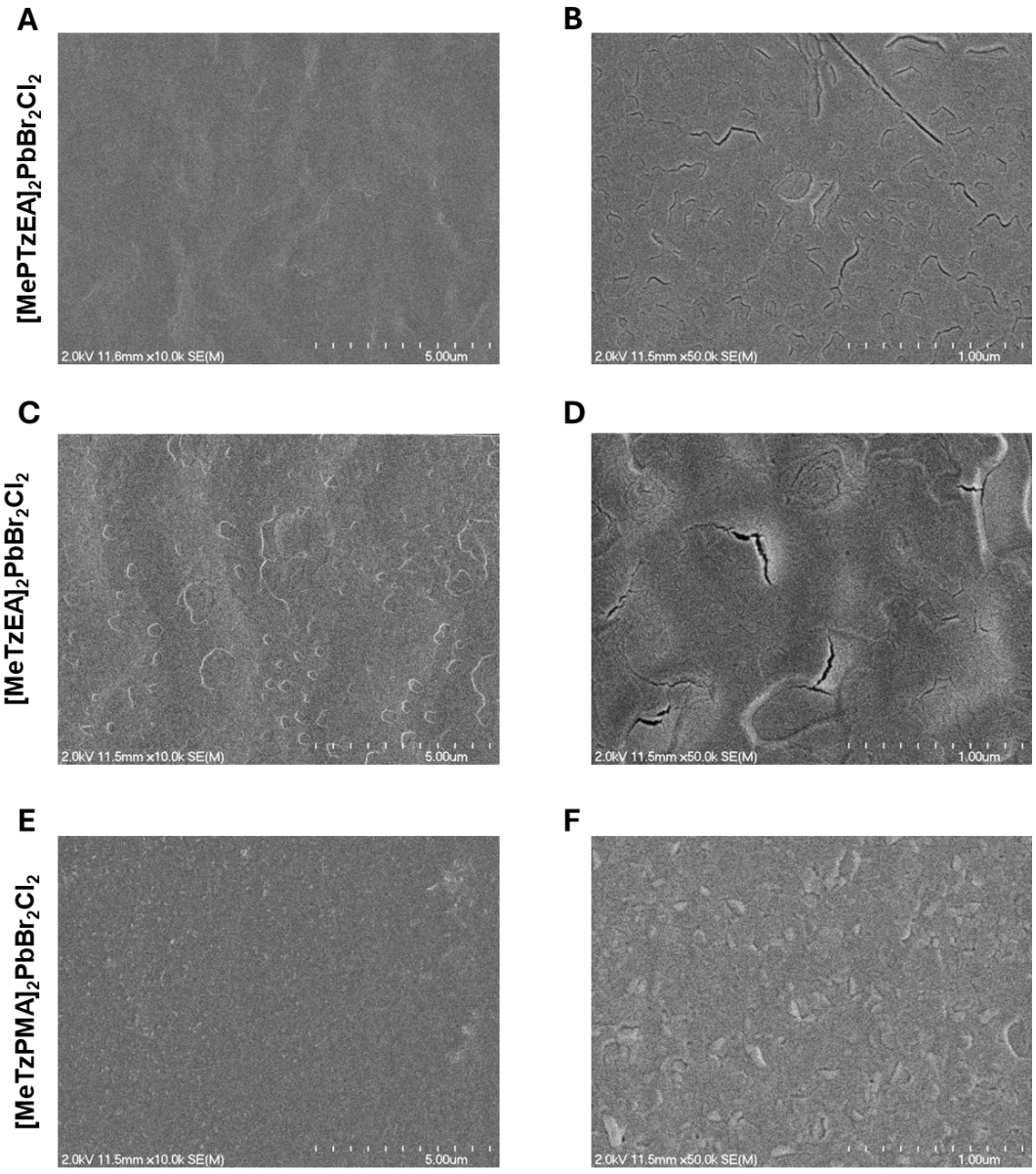

Figure S19 | Scanning electron microscopy (SEM) images of mixed-anion films. $[MePTzEA]_2PbBr_2Cl_2$ at (A) 10k and (B) 50k magnification. $[MeTzEA]_2PbBr_2Cl_2$ at (C) 10k and (D) 50k magnification. $[MeTzPMA]_2PbBr_2Cl_2$ at (E) 10k and (F) 50k magnification.

5. Crystallographic Tables

Table S2 | Crystal data and structure refinement for $[MeTzEA]_2PbCl_4$

Empirical formula	C5 H10 Cl2 N5 Pb0.5	
Formula weight	314.67	
Crystal color, shape, size	purple plate, 0.080 x 0.080 x 0.005 mm^3	
Temperature	150 K	
Wavelength	0.71073 Å	
Crystal system, space group	Monoclinic, C2/m	
Unit cell dimensions	a = 7.8434(7) Å	α = 90°
	b = 31.616(4) Å	β = 133.850(2)°
	c = 5.6370(5) Å	γ = 90°
Volume	1008.06(17) $Å^3$	
Z	4	
Density (calculated)	2.073 Mg/m^3	
Absorption coefficient	8.915 mm^{-1}	
F(000)	600	
Diffractometer	Bruker D8 VENTURE, Bruker	
Theta range for data collection	2.577 to 25.134°.	
Index ranges	-9<=h<=9, -37<=k<=37, -6<=l<=6	
Reflections collected	10714	
Independent reflections	931 [R(int) = 0.125]	
Observed Reflections	893	
Completeness to theta = 25.134°	99.8 %	
Absorption correction	Semi-empirical from equivalents	
Max. and min. transmission	0.96 and 0.49	
Solution	Charge Flipping methods	
Refinement method	Full-matrix least-squares on F^2	
Weighting scheme	$w = [s^2Fo^2 + AP^2 + BP]^{-1}$, with	
	$P = (Fo^2 + 2\,Fc^2)/3$, A = 0.06, B = 21.46	
Data / restraints / parameters	928 / 87 / 128	
Goodness-of-fit on F^2	1.0430	
Final R indices [I>2sigma(I)]	R1 = 0.0431, wR2 = 0.1090	
R indices (all data)	R1 = 0.0461, wR2 = 0.1125	
Largest diff. peak and hole	1.75 and -1.85 $e.Å^{-3}$	

Table S3 | Crystal data and structure refinement for $[MeTzPMA]_2PbCl_4 \cdot CH_2Cl_2$

Empirical formula	C21 H26 Cl6 N10 Pb1
Formula weight	838.42
Crystal color, shape, size	purple block, 0.150 x 0.100 x 0.070 mm^3
Temperature	150 K
Wavelength	1.54178 Å
Crystal system, space group	Orthorhombic, $Pca2_1$
Unit cell dimensions	a = 15.675(3) Å α = 90°
	b = 25.755(6) Å β = 90°
	c = 7.6296(13) Å γ = 90°
Volume	3080.1(11) $Å^3$
Z	4
Density (calculated)	1.808 Mg/m^3
Absorption coefficient	15.697 mm^{-1}
F(000)	1624
Diffractometer	Bruker D8 VENTURE, Bruker
Theta range for data collection	1.715 to 81.528°.
Index ranges	-19<=h<=17, -32<=k<=32, -9<=l<=9
Reflections collected	43488
Independent reflections	6513 [R(int) = 0.211]
Observed Reflections	3300
Completeness to theta = 79.082°	99.6 %
Absorption correction	Semi-empirical from equivalents
Max. and min. transmission	0.33 and 0.21
Solution	Intrinsic phasing methods
Refinement method	Full-matrix least-squares on F^2
Weighting scheme	$w = [s^2Fo^2 + AP^2 + BP]^{-1}$, with
	$P = (Fo^2 + 2\,Fc^2)/3$, A = 0.080, B = 0.000
Data / restraints / parameters	6513 / 315 / 367
Goodness-of-fit on F^2	0.9684
Final R indices [I>2sigma(I)]	R1 = 0.0866, wR2 = 0.2007
R indices (all data)	R1 = 0.1454, wR2 = 0.2679
Absolute structure parameter	0.02(2)
Largest diff. peak and hole	3.06 and -2.66 $e.Å^{-3}$

Table S4 | Crystal data and structure refinement for $[MePTzEA]_2PbCl_4$

Empirical formula	C22 H28 Cl4 N10 Pb1	
Formula weight	781.54	
Crystal color, shape, size	pink plate, 0.100 x 0.050 x 0.005 mm^3	
Temperature	150 K	
Wavelength	0.71073 Å	
Crystal system, space group	Monoclinic, C 1 c 1	
Unit cell dimensions	a = 47.562(12) Å	α = 90°
	b = 7.8595(15) Å	β = 96.530(7)°
	c = 7.675(2) Å	γ = 90°
Volume	2850.2(12) $Å^3$	
Z	4	
Density (calculated)	1.821 Mg/m^3	
Absorption coefficient	6.326 mm^{-1}	
F(000)	1520	
Diffractometer	Bruker D8 VENTURE, Bruker	
Theta range for data collection	2.586 to 25.027°	
Index ranges	-56<=h<=56, -8<=k<=9, -9<=l<=9	
Reflections collected	19612	
Independent reflections	4938 [R(int) = 0.164]	
Observed Reflections	4005	
Completeness to theta = 25.027°	99.3 %	
Absorption correction	Semi-empirical from equivalents	
Max. and min. transmission	0.97 and 0.73	
Solution	Intrinsic phasing methods	
Refinement method	Full-matrix least-squares on F^2	
Weighting scheme	$w = [s^2Fo^2 + AP^2 + BP]^{-1}$, with	
	$P = (Fo^2 + 2\,Fc^2)/3$, A = 0.11, B = 1.36	
Data / restraints / parameters	4919 / 330 / 358	
Goodness-of-fit on F^2	0.9944	
Final R indices [I>2sigma(I)]	R1 = 0.0781, wR2 = 0.1829	
R indices (all data)	R1 = 0.0918, wR2 = 0.1980	
Largest diff. peak and hole	5.46 and -2.16 $e.Å^{-3}$	

Table S5 | Crystal data and structure refinement for $[BA]_2PbBr_2Cl_2$

Empirical formula	C8 H24 Br2 Cl2 N2 Pb1	
Formula weight	586.21	
Crystal color, shape, size	colorless plate, 0.040 x 0.040 x 0.005 mm^3	
Temperature	150 K	
Wavelength	0.71073 Å	
Crystal system, space group	Tetragonal, I4/m	
Unit cell dimensions	a = 5.6345(3) Å	α = 90°
	b = 5.6345(3) Å	β = 90°
	c = 27.4825(19) Å	γ = 90°
Volume	872.50(11) $Å^3$	
Z	2	
Density (calculated)	2.231 Mg/m^3	
Absorption coefficient	14.533 mm^{-1}	
F(000)	544	
Diffractometer	Bruker D8 VENTURE, Bruker	
Theta range for data collection	2.965 to 36.233°	
Index ranges	-8<=h<=9, -8<=k<=9, -45<=l<=45	
Reflections collected	13525	
Independent reflections	1075 [R(int) = 0.056]	
Observed Reflections	1073	
Completeness to theta = 34.784°	99.7 %	
Absorption correction	Semi-empirical from equivalents	
Max. and min. transmission	0.93 and 0.56	
Solution	Intrinsic phasing methods	
Refinement method	Full-matrix least-squares on F^2	
Weighting scheme	$w = [s^2Fo^2 + AP^2 + BP]^{-1}$, with	
	$P = (Fo^2 + 2\,Fc^2)/3$, A = 0.080, B = 84.680	
Data / restraints / parameters	1073 / 43 / 50	
Goodness-of-fit on F^2	1.0130	
Final R indices [I>2sigma(I)]	R1 = 0.0756, wR2 = 0.1863	
R indices (all data)	R1 = 0.0756, wR2 = 0.1863	
Largest diff. peak and hole	6.55 and -13.10 $e.Å^{-3}$	

Table S6 | Crystal data and structure refinement for $[MeTzEA]_2PbBr_2Cl_2$

Empirical formula	C5 H10 Br1 Cl1 N5 Pb0.50
Formula weight	359.12
Crystal color, shape, size	purple plate, 0.080 x 0.060 x 0.005 mm^3
Temperature	150 K
Wavelength	0.71073 Å
Crystal system, space group	Tetragonal, I-4
Unit cell dimensions	a = 5.66250(10) Å α = 90°
	b = 5.66250(10) Å β = 90°
	c = 31.9410(15) Å γ = 90°
Volume	1024.15(6) $Å^3$
Z	4
Density (calculated)	2.329 Mg/m^3
Absorption coefficient	12.416 mm^{-1}
F(000)	672
Diffractometer	Bruker D8 VENTURE, Bruker
Theta range for data collection	2.551 to 30.610°.
Index ranges	-8<=h<=8, -8<=k<=8, -45<=l<=45
Reflections collected	14347
Independent reflections	1583 [R(int) = 0.073]
Observed Reflections	1576
Completeness to theta = 29.998°	99.9 %
Absorption correction	Semi-empirical from equivalents
Max. and min. transmission	0.94 and 0.47
Solution	Intrinsic phasing methods
Refinement method	Full-matrix least-squares on F2
Weighting scheme	$w = [s^2Fo^2 + AP^2 + BP]^{-1}$, with
	$P = (Fo^2 + 2\,Fc^2)/3$, A = 0.147, B = 23.130
Data / restraints / parameters	1583 / 131 / 118
Goodness-of-fit on F^2	1.0222
Final R indices [I>2sigma(I)]	R1 = 0.0659, wR2 = 0.1834
R indices (all data)	R1 = 0.0661, wR2 = 0.1837
Absolute structure parameter	0.472(10)
Largest diff. peak and hole	2.54 and -3.52 $e.Å^{-3}$

6. Electronic Structure Calculations

For $[MePTzEA]_2PbCl_4$, experimentally-measured XRD structure is available. We perform first-principles electronic structure calculation based on the density functional theory calculations using the all-electron FHI-aims code[10] as described in our work.[11] To be consistent with the measured experimental structures, a $c(2 \times 2) \times 2$ lateral supercell is used for all the calculations, having 260 atoms (1520 electrons), with the Brillouin zone (BZ) sampling of $1 \times 6 \times 6$ k-points. Geometry optimization is performed with Perdew–Burke-Ernzerhof (PBE) exchange-correlation (XC)[12] functional together with the Tkatchenko-Scheffler (TS) pairwise dispersion correction,[13] with the residual energy tolerance of 0.002 eV. Using the optimized structure, we calculate the electronic structure using the Heyd–Scuseria–Ernzerhof (HSE06)[14] hybrid XC functional, with the default parameters $\alpha = 0.25$ and $\omega = 0.11$ bohr^{-1}, including spin orbit coupling (SOC) with the non-self-consistent perturbative approach[15] with a BZ sampling of $1 \times 6 \times 6$. We use "tight" basis set setting and "intermediate" basis set settings for geometry relaxation and band structure calculations as implemented in FHI-aims code.[10, 16]

The optimized structures agree with the experimental measurements within 0.1%, 0.3 % for ***b*** and ***c*** lattice parameters and within 1.8 % for the ***a*** lattice parameters, ***a*** being the out of plane lattice vector. **Figure S20A** shows the mutual alignment of the $-NH_3$ cation with respect to the inorganic layer. The arrows highlight the direction of tilting of $-NH_3$ hence affecting the hydrogen bond interaction with inorganic cage.[11] **Figure S20B** shows the two sets of equatorial Pb-I-Pb bond angles with values 138.12° and 150.96°. These Pb-I-Pb bond angles confirm the absence of inversion symmetry in the inorganic sublattice. The overall space group as calculated from the relaxed structure is Cc, computed using Spglib[17] with a threshold of 6E-5 Å and corroborates with the space group computed from XRD geometry. **Figure S20C-D** shows the band structure along the high symmetry path with band Mulliken population accounting for contribution from organic/inorganic layer and inorganic layer respectively. **Figure S20E** shows the density of states (DOS) In **Figure S20C** organic layer forms the conduction bands while the valence band edges are contributed from inorganic sub lattice, making $[MePTzEA]_2PbBr_2Cl_2$ to possess a novel Type IIa quantum well arrangement.[16] We observe the direct band gap of 1.73 eV at the Γ point, and since the frontier band edges are not influenced by Pb atoms, the incorporation of SOC does not result in a significant change to the band gap. Additionally, we observe a unidirectional band splitting in the conduction bands with higher Pb atom contribution from inorganic layer, as shown in **Figure S20D.** This can be attributed to the absence of a center of inversion, as indicated by the Pb-I-Pb bond angles. Such spin-splitting is also been observed in other 2D-HOIPs systems,[11] although exploring the relativistic effects in these systems is beyond the scope of this work. In **Figure S20E**, we further show the overall energy level alignment of organic and inorganic layer for $[MePTzEA]_2PbBr_2Cl_2$ calculated using band Mulliken charge analysis.[16] The band structure shows a Type IIa quantum well alignment, with a 2.95 eV difference between the CBM and VBM energies of the organic layers. For inorganic layer CBM and VBM energy difference is 3.43 eV as shown in **Figure S20E**. While it forms a Type IIa alignment, both organic and inorganics -

derived states exist near the valence band minimum (**Figure S20D**), making it a rather unique case among the the Type IIa alignment.[18] For other structures ($[MeTzEA]_2PbCl_4$ and $[MeTzPMA]_2PbCl_4{\cdot}CH_2Cl_2$) well-resolved XRD structures could not be obtained, and DFT calculations were not performed.

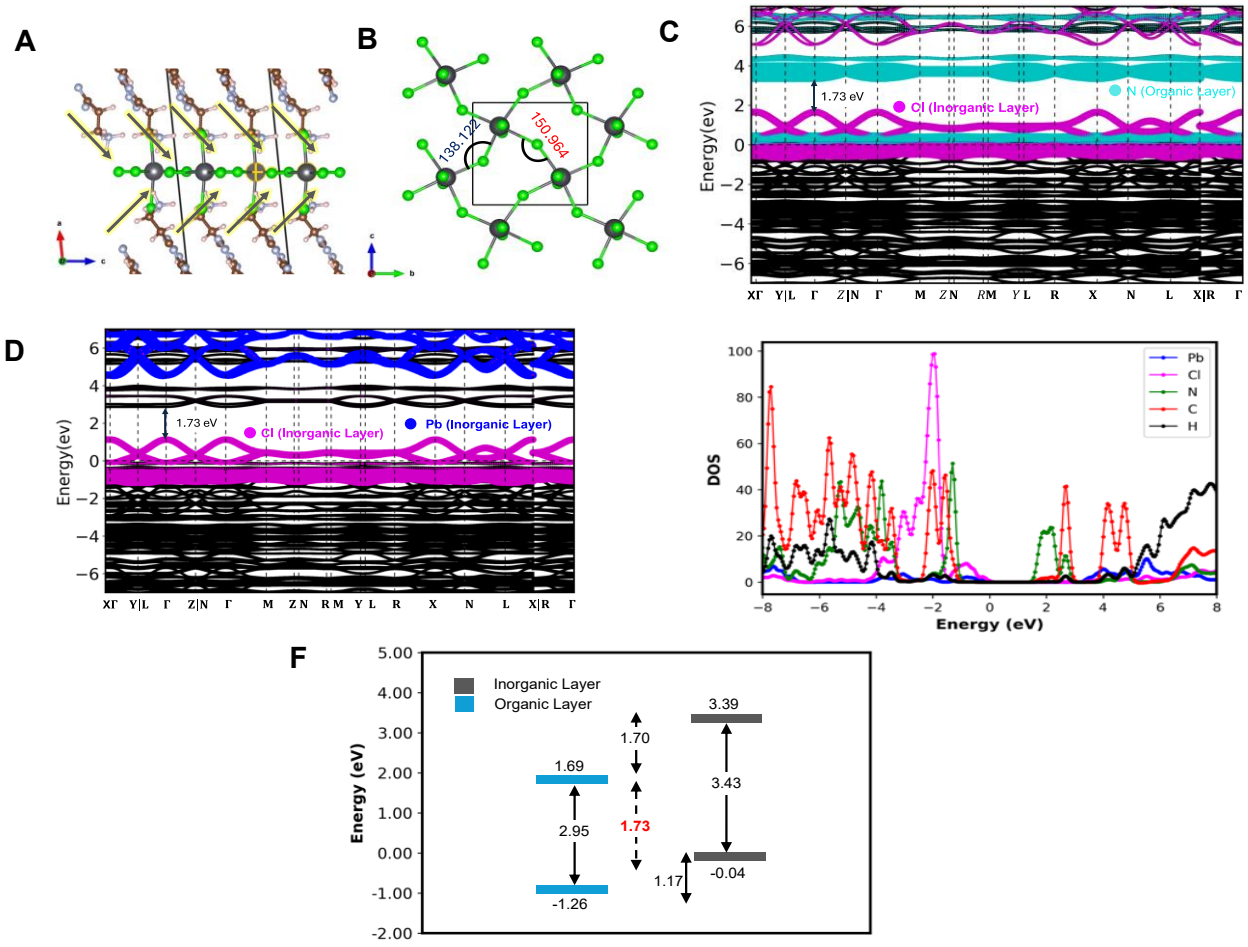

Figure S20 | Computational details and findings. (A) alignment of the ammonium (-$NH3^+$) group in organic sublayer, yellow arrows indicate the relative arrangement of the ammonium group with respect to inorganic lattice for $[MePTzEA]_2PbCl_4$.. (B) Inorganic cage corresponding to relaxed structure, insets showing two kinds of Pb-I-Pb observed in $[MePTzEA]_2PbCl_4$. (C)-(D) Band structure plots for $[MePTzEA]_2PbCl_4$. Turquoise, magenta and blue show contribution of N,Cl and Pb respectively. (E) Density of states (DOS) calculated using HSE06+SOC, insets showing colors corresponding to the atom. (F) Energy level alignment shown for organic (blue) and inorganic (gray) layers corresponding Type IIa quantum well. Band gap of 1.73 eV is shown in red.

7. Band Alignment Measurements

For ultraviolet photoelectron spectroscopy (UPS) measurements, thin films of the samples were spin coated onto silicon wafers. The fabrication process for BA-based perovskites was identical to the thin film fabrication above. The tetrazine cation samples had a concentration of 0.6 M in DMSO and were spin coated onto silicon wafers at 3000 rpm for 30 seconds, followed by 10 minutes of thermal annealing at 100 °C. X-ray photoelectron spectroscopy (XPS) data was collected on a Kratos Supra+ system with a monochromatic Kα x-ray source operated at 150W. A charge neutralizer was used to prevent charging when necessary and all spectra were corrected to the C 1s peak at 284.6 eV. Survey and high-resolution scans were acquired at pass energies of 80 eV and 20 eV, respectively, and the analyzed spot size was 300 x 700 um. Kratos ESCApe software was used for data analysis, Shirley baselines were used, and the relative sensitivity factors used for quantification were those from the ESCApe software. Ultraviolet photoelectron spectroscopy (UPS) data was collected on the same Kratos Supra+ system. A He I UV source was used and operated at 20 mA. Data was acquired in UPS lens mode, with a pass energy of 5 eV and an aperture of 55 um. A -9V bias was applied to the sample.

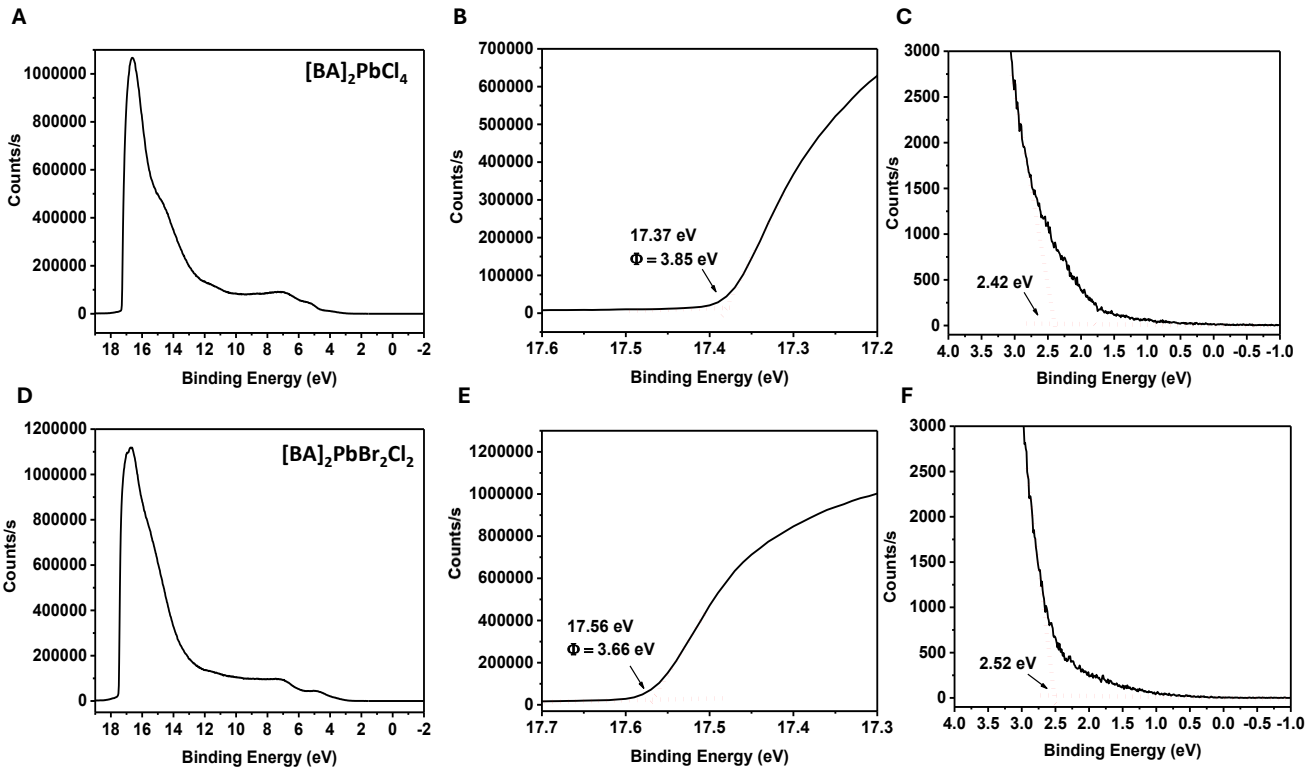

Figure S21 | UPS spectra for the inorganic layers. (A) Full spectra, (B) work function, and (C) valence band edge for $[BA]_2PbCl_4$. (A) Full spectra, (B) work function, and (C) valence band edge for $[BA]_2PbBr_2Cl_2$.

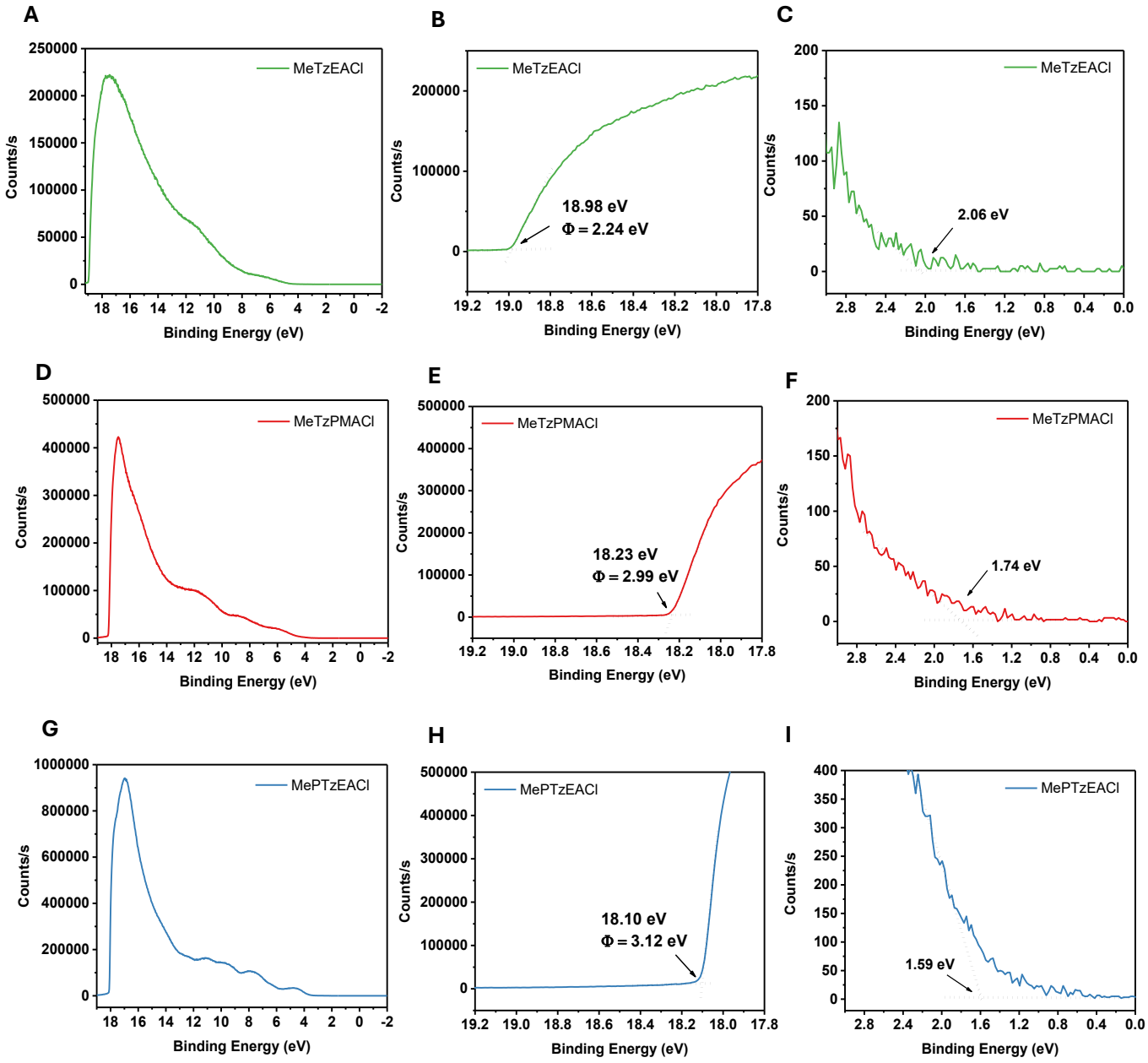

Figure S22 | UPS spectra for the organic layers. (A) Full spectra, (B) HOMO, and (C) work function for MeTzEACl (green). (D) Full spectra, (E) HOMO, and (F) work function for MeTzPMACl (red). (G) Full spectra, (H) HOMO, and (I) work function for MePTzEACl (blue).

8. Optical Spectroscopies

8.1 UV-Vis Absorbance

Solution and thin film absorption spectra were acquired with a Shimadzu UV-2600 spectrometer.

8.2 Steady State Photoluminescence

Steady-state photoluminescence (PL) emission and excitation spectra of both solutions and films were acquired using an Edinburgh FLS920 spectrometer. Solution samples were measured in a 1 cm × 1 cm quartz cuvette, while film samples were mounted on a sample holder with fine positional adjustment to optimize PL intensity.

Steady state PL emission spectra were measured with excitation wavelengths of 320 or 510 nm, each with a bandwidth of 10 nm. Emitted light was collected using a 0.5-nm detection bandwidth and scanned with a step size of 1 nm. To minimize scattered excitation light, two pieces of color glass filters (Thorlabs, FGB37) were placed before the spectrograph slit for excitation at 320 nm. Two 550-nm long-pass filters (Thorlabs, FELH0550) were used for measurement with excitation wavelengths of 375 and 510 nm.

Excitation spectra were measured with the emission wavelength fixed at 600 nm and a 10 nm emission bandwidth. Excitation wavelength was scanned from 330 nm to 550 nm using a 1.5 nm excitation bandwidth and a 2 nm step size. Two 550 nm long-pass filters (Thorlabs, FELH0550) were also placed before the spectrograph slit to suppress scattered excitation light.

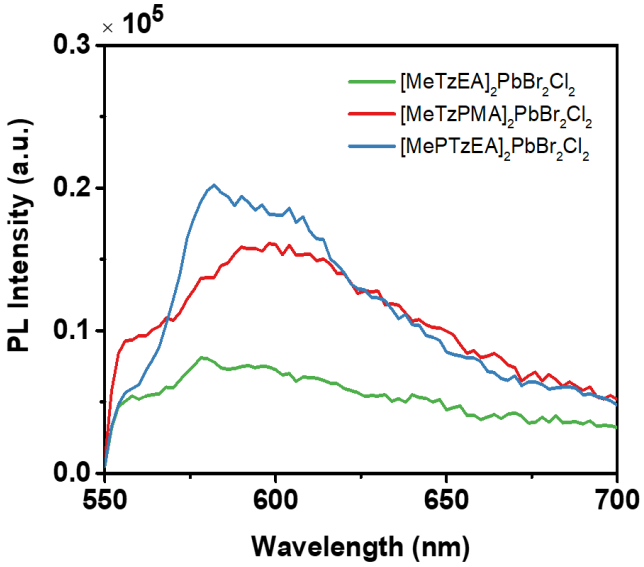

Figure S23 | Photoluminescene (PL) spectra for $[MeTzEA]_2PbBr_2Cl_2$ (green), $[MeTzPMA]_2PbBr_2Cl_2$ (red), and $[MePTzEA]_2PbBr_2Cl_2$ (blue) films excited at 375 nm, measured at the tetrazine emission 550 – 700 nm. 375 nm excitation was chosen to selectively excite the inorganic exciton while minimizing direct

excitation of the tetrazine n - π* transition.

8.3 Transient Grating

Transient grating experiments were conducted using a Coherent Libra titanium-sapphire laser system producing 3.5-mJ, 50-fs pulses at 1 kHz. Approximately half of the 800-nm fundamental output was focused into a 4-meter tube filled with argon gas at an absolute pressure of 1.5 atm to generate a visible continuum. From this continuum, the near-infrared portion of the beam was separated using an 800-nm beamsplitter and directed to generate ultraviolet light through second harmonic generation (SHG). To prevent optical damage from the 800-nm light, a 760-nm long-pass dichroic mirror was employed to effectively dump the intense fundamental component. By focusing the filtered near-infrared beam onto a 1-mm thick beta barium borate (BBO) crystal (Castech, $\theta = 32°$) using a 20-cm focal length lens, a 375-nm pulse with an energy of approximately 450 nJ and a spectral bandwidth of 4 nm (FWHM) was obtained.

This beam was subsequently split into two pulses using a beamsplitter. One pulse traveled along a fixed optical path, while the other was delayed using retroreflectors (Newport, UBBR2.5-2UV) mounted on motorized translation stages (Newport, GTS 150) with 15-cm travel ranges. As shown in **Figure S24A**, both pulses were focused onto diffractive optics (Holoeye) using a 50-cm focal length silver-coated mirror. At 375 nm, the ±1 diffraction orders were separated from the zeroth-order beam by 1.9°. These diffracted beams were relayed to the sample using two 20-cm focal length, 7.5-cm diameter silver-coated spherical mirrors.

At the sample position, all four laser pulses were focused to approximately 170 μm FWHM. The first two pulses ($\mathbf{k_1}$, $\mathbf{k_2}$) had energies of 24 nJ, while the energy of the third pulse ($\mathbf{k_3}$) was 8 nJ. The four pulses form a square grid geometry, as shown in **Figure S24B**. Transient grating signals were generated under phase matching condition beam ($\mathbf{k_{signal} = k_1 - k_2 + k_3}$) and were detected via spectral interferometry. The detection scheme was enabled by the collinear geometry of the signal and the local oscillator, which was attenuated and delayed relative to the probe pulse ($\mathbf{k_3}$) using neutral density filter paper and microscope coverslips.[19-26] Transient grating signals acquired using dimethyl sulfoxide, contained in a 1-mm-thick cuvette, yield instrument response widths of approximately 100 fs.

Signal detection was carried out using a homebuilt Czerny–Turner spectrograph, which incorporated two 20-cm focal length silver-coated mirrors and a 2400-grooves/mm diffraction grating. The interferograms were detected by a 12-bit monochrome CMOS camera (Thorlabs, CS95MU) with 100-ms integration times. Signal fields were subsequently extracted using standard Fourier transform filtering algorithms.[24-28]

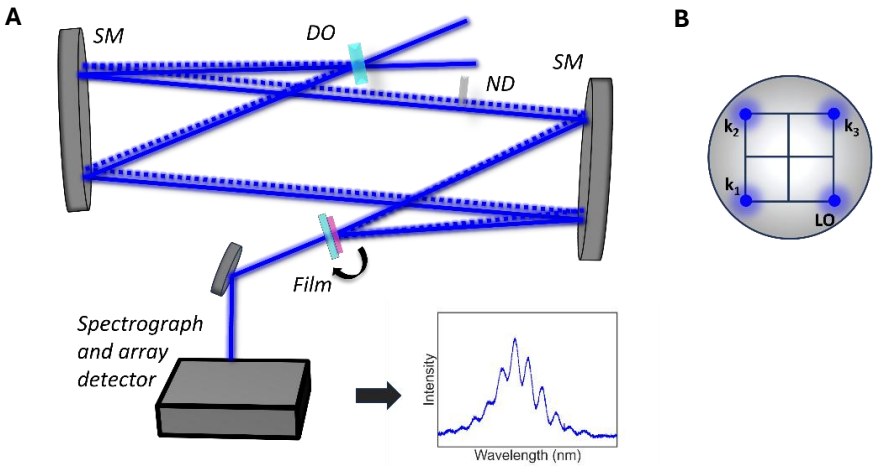

Figure S24 | (A) Transient grating experiments are conducted with a four-beam diffractive optic-based interferometer. Signals are detected by spectral interferometry with a Czerny-Turner spectrograph and CMOS sensor. (B) Square grid geometry formed by the four beams enables third-order nonlinear spectroscopies with $\mathbf{k}_{signal} = \mathbf{k}_1 - \mathbf{k}_2 + \mathbf{k}_3$ phase-matching conditions.

During the data acquisition, two-dimensional perovskite films were continuously rotated using a mechanical stage (Zaber, X-RSW60A-E03-KX13A), sweeping a 1-cm diameter circle on the film surface to minimize local heating and improve signal averaging.[26] Delay times between pulses were scanned over a 515-ps range using a logarithmic scale to enhance resolution at shorter delays and better capture fast decay dynamics. Each scan was repeated 20–60 times over 20–60 minutes to optimize signal-to-noise ratios. No degradation of perovskite films was observed, as evidenced by the consistent signal strength throughout the measurements.

Transient grating measurements were repeated twice with the same experimental conditions on perovskite samples spin-coated in the same batch. Consistent results are displayed in **Figure S25**. The timescale of the excited state dynamics discussed in this paper was evaluated by averaging over these two experimental results.

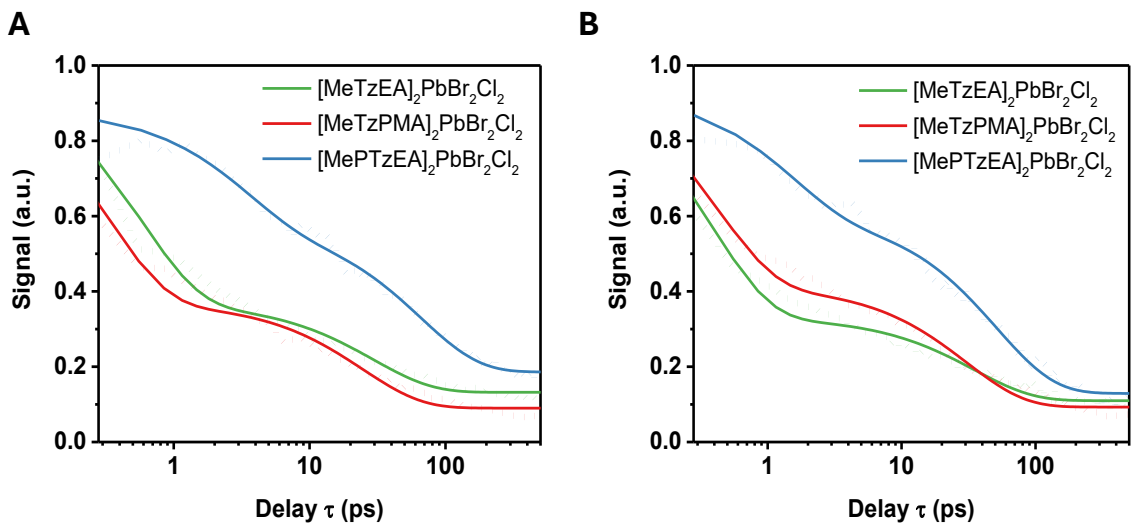

Figure S25 | (A), (B) Dotted line: experimentally measured transient grating signal. Solid line: fitting curve using **Equation (1)**. Two independent transient grating experiments were conducted to prove consistency and reproducibility. Both measurements showed that the $[MePTzEA]_2PbBr_2Cl_2$ experienced much slower relaxation in the excited states.

9. Perturbative Models for Quenching Mechanisms

We propose that excited-state quenching occurs via energy- and charge-transfer mechanisms. While transient-grating measurements provide time scales, the fluorescence-excitation spectra are essential for determining whether energy- or charge-transfer quenching dominates in each system.

9.1 Dexter Energy Transfer

Here, we outline a derivation of the Dexter energy-transfer rate formula to clarify the role of empirical parameters. It is instructive to obtain a formula consistent with the Marcus model for electron transfer, which is used to interpret concomitant charge-transfer quenching processes. The system Hamiltonian is expressed using a minimal direct-product basis of electronic excitations of the donor and acceptor:

$$\hat{H}_{sys} = |e_D g_A\rangle E_D \langle e_D g_A| + |g_D e_A\rangle E_A \langle g_D e_A| \ , \tag{1}$$

where E_D and E_A are the mean values of the energy gaps for the donor and acceptor respectively. In the present model, these energy gaps correspond to the electronic origins (isosbestic points between absorbance and fluorescence spectra). To begin, we express the rate constant using a time-correlation function for the Dexter coupling between the donor and acceptor:

$$k_{Dexter} = \frac{1}{\hbar^2}\int_{-\infty}^{\infty} dt \left\langle e_D g_A \left| \hat{H}_{Dexter}(t)\hat{H}_{Dexter}(0) \right| e_D g_A \right\rangle . \tag{2}$$

Aside from the definition of the perturbative coupling, the derivation from this point closely follows that associated with the Förster model. Using closure, the integrand is given by a product of matrix elements:

$$k_{Dexter} = \frac{1}{\hbar^2}\int_{-\infty}^{\infty} dt \left\langle e_D g_A \left| \hat{H}_{Dexter}(t) \right| g_D e_A \right\rangle \left\langle g_D e_A \left| \hat{H}_{Dexter}(0) \right| e_D g_A \right\rangle \tag{3}$$

At this stage, energy level fluctuations are typically introduced in the derivation of perturbative rate formulas via cumulant expansions. Gaussian spectral line shapes may then be obtained under the assumption of slowly modulated energy level fluctuations. This approach has been applied to several types of non-radiative transitions (e.g., electron transfer, spin relaxation, internal conversion, etc.). The rate is then written as a product of dephasing profiles for the donor and acceptor resonances:

$$\begin{aligned} k_{Dexter} &= \frac{\left| \left\langle e_D g_A \left| \hat{H}_{Dexter} \right| g_D e_A \right\rangle \right|^2}{\hbar^2} \\ &\times \int_{-\infty}^{\infty} dt \exp\left[i\frac{\left(E_D - \lambda_D\right)}{\hbar}t - \frac{\lambda_D k_B T}{\hbar^2}t^2 \right] \exp\left[-i\frac{\left(E_A + \lambda_A\right)}{\hbar}t - \frac{\lambda_A k_B T}{\hbar^2}t^2 \right] \end{aligned} \tag{4}$$

where the donor and acceptor resonances are centered at their excited-state and ground-state free-energy minima, respectively. To write the product of dephasing profiles, we note the following relationship in the Heisenberg picture with respect to the zeroth-order Hamiltonian:

$$\begin{aligned} \left\langle e_D g_A \left| \hat{H}_{Dexter}(t) \right| g_D e_A \right\rangle &= \left\langle e_D g_A \left| \exp\left(i\hat{H}_0 t/\hbar \right) \hat{H}_{Dexter} \exp\left(-i\hat{H}_0 t/\hbar \right) \right| g_D e_A \right\rangle \\ &= \exp\left[i\frac{\left(E_D - \lambda_D\right)}{\hbar}t - \frac{\lambda_D k_B T}{\hbar^2}t^2 \right] \exp\left[-i\frac{\left(E_A + \lambda_A\right)}{\hbar}t - \frac{\lambda_A k_B T}{\hbar^2}t^2 \right] \end{aligned} \tag{5}$$

Parseval's theorem is then used to introduce the normalized spectral overlap between the donor and acceptor line shapes:

$$\begin{aligned} k_{Dexter} &= \frac{\left| \left\langle e_D g_A \left| \hat{H}_{Dexter} \right| g_D e_A \right\rangle \right|^2}{\hbar^2} \\ &\times \frac{\hbar}{2k_B T\sqrt{\lambda_D \lambda_A}} \int_{-\infty}^{\infty} dE \exp\left[-\frac{\left(E - E_D + \lambda_D\right)^2}{4\lambda_D k_B T} \right] \exp\left[-\frac{\left(E - E_A - \lambda_A\right)^2}{4\lambda_A k_B T} \right] \end{aligned} \tag{6}$$

Evaluation of the spectral overlap yields

$$k_{Dexter} = \left|\left\langle e_D g_A \left| \hat{H}_{Dexter} \right| g_D e_A \right\rangle\right|^2 \times \sqrt{\frac{\pi}{\hbar^2 k_B T \left(\lambda_D + \lambda_A\right)}} \exp\left[-\frac{\left(E_D - \lambda_D - E_A - \lambda_A\right)^2}{4\left(\lambda_D + \lambda_A\right) k_B T} \right] \cdot \quad (7)$$

To facilitate interpretation of the experimental data, we next simplify this expression by assuming degenerate donor and acceptor energy gaps $E_D - \lambda_D - E_A - \lambda_A \approx 0$:

$$k_{Dexter} = \left|\left\langle e_D g_A \left| \hat{H}_{Dexter} \right| g_D e_A \right\rangle\right|^2 \sqrt{\frac{\pi}{\hbar^2 k_B T \left(\lambda_D + \lambda_A\right)}} \cdot \quad (8)$$

In addition, we further denote the Dexter coupling as $V_{Dexter} \equiv \left\langle e_D g_A \left| \hat{H}_{Dexter} \right| g_D e_A \right\rangle$ to simplify the notation for the comparison of quenching mechanisms below. The Dexter coupling can be expressed using the empirical quenching time as

$$V_{Dexter} = \left(\frac{\hbar^2 k_B T \left(\lambda_D + \lambda_A\right)}{\pi t_{quench}^2} \right)^{1/4} \cdot \quad (9)$$

To obtain empirical coupling strengths, the reorganization energies of the perovskite donor, MeTzEA and MeTzPMA acceptors are set equal to 110, 90 and 100 meV, respectively. These values correspond to half of the Stokes shifts in the steady-state absorption spectra and fluorescence spectra. For the perovskite, the Stokes shift is estimated using the absorbance and fluorescence spectra of $[BA]_2PbBr_2Cl_2$, while assuming that the reorganization energy of the inorganic layer is insensitive to the organic cations. The Stokes shifts for tetrazine spacer cations are computed using the absorption and fluorescence spectra associated with the n-π* transitions.

9.2 Charge Transfer

While band alignment at the inorganic-organic interface is not required for energy transfer, charge transfer quenching requires that the inorganic and organic systems have nearly degenerate energy levels. According to the UPS results, the HOMO orbitals of the tetrazine molecules have energies more than 0.4 eV greater than the valence band of the perovskite. Therefore, it is most likely that the acceptor states for hole transfer involve lower energy occupied molecular orbitals within the tetrazine systems, as indicated in **Figure 8**.

Under the assumption that one of the occupied molecule orbitals of MePTzEA coincides with the valence band of the perovskite, we estimate the donor-acceptor coupling using the Marcus equation for barrierless process:

$$k_{Marcus} = \sqrt{\frac{\pi}{\hbar^2 \lambda k_B T}} \left| \left\langle \psi_D \left| \hat{H}_{Marcus} \right| \psi_A \right\rangle \right|^2 , \tag{10}$$

where the λ is the reorganization energy for the transition, and $\left\langle \psi_D \left| \hat{H}_{Marcus} \right| \psi_A \right\rangle$ is the coupling between the donor and acceptor's orbitals. To simplify the discussion of Dexter and Marcus relaxation mechanisms, we hereafter denote the donor-acceptor coupling for charge transfer as $V_{Marcus} \equiv \left\langle \psi_D \left| \hat{H}_{Marcus} \right| \psi_A \right\rangle$. Notably, the reorganization energy associated with charge transfer corresponds to the energy gap between the levels of the donor and acceptor and cannot be derived directly from spectroscopic line widths or Stokes shifts. Therefore, we equate the reorganization energy to k_BT and approximate the rate using the inverse of the empirical quenching time:

$$V_{Marcus} \approx \pi^{-1/4} \sqrt{\frac{\hbar k_B T}{t_{quench}}} , \tag{11}$$

The donor-acceptor couplings computed for the various systems are summarized in **Table S7**. The quenching times t_{quench} are obtained from the transient grating measurements described in the main text and used to evaluate **Equations (9) and (11)**. The reorganization energy parameters are provided in the above text.

Table S7 | Empirical Dexter and Marcus couplings

Parameters	$[MePTzEA]_2PbBr_2Cl_2$	$[MeTzPMA]_2PbBr_2Cl_2$	$[MeTzEA]_2PbBr_2Cl_2$
[a] t_{quench} (ps)	25.993±1.005	8.523±0.331	7.684±0.358
[b] V_{Dexter} (meV)	----------	1.789	1.861
[b] V_{Marcus} (meV)	0.606	----------	----------

[a] The empirical quenching times are obtained by fitting transient grating signals. See main text for summary of fitting parameters.

[b] The Dexter and Marcus couplings are computed using **Equations (9) and (11)** with k_BT set equal to. 25.7 meV.

10. References

1. Mao, W.; Shi, W.; Li, J.; Su, D.; Wang, X.; Zhang, L.; Pan, L.; Wu, X.; Wu, H., Organocatalytic and Scalable Syntheses of Unsymmetrical 1,2,4,5-Tetrazines by Thiol-Containing Promotors. *Angewandte Chemie International Edition* **2019,** *58* (4), 1106-1109.

2. Zhao, X.; Liu, T.; Kaplan, A. B.; Yao, C.; Loo, Y.-L., Accessing Highly Oriented Two-Dimensional Perovskite Films via Solvent-Vapor Annealing for Efficient and Stable Solar Cells. *Nano Letters* **2020,** *20* (12), 8880-8889.

3. Liu, J.; Ozaki, M.; Yakumaru, S.; Handa, T.; Nishikubo, R.; Kanemitsu, Y.; Saeki, A.; Murata, Y.; Murdey, R.; Wakamiya, A., Lead-Free Solar Cells based on Tin Halide Perovskite Films with High Coverage and Improved Aggregation. *Angewandte Chemie International Edition* **2018,** *57* (40), 13221-13225.
4. Sun, X.; Han, C.; Liu, Z.; Xu, L.; Li, J.; Yu, H.; Wang, K., Effectiveness of Solvent Vapor Annealing on Optoelectronic Properties for Quasi-2D Organic–Inorganic Hybrid Perovskite Light-Emitting Diodes. *The Journal of Physical Chemistry C* **2020,** *124* (52), 28417-28423.
5. SAINT, Bruker Analytical X-Ray Systems. *Madison WI*.
6. Blessing, R., An empirical correction for absorption anisotropy. *Acta Crystallographica Section A* **1995,** *51* (1), 33-38.
7. Altomare, A.; Cascarano, G.; Giacovazzo, C.; Guagliardi, A.; Burla, M. C.; Polidori, G.; Camalli, M., SIR92 - a program for automatic solution of crystal structures by direct methods. *Journal of Applied Crystallography* **1994,** *27* (3), 435.
8. Betteridge, P. W.; Carruthers, J. R.; Cooper, R. I.; Prout, K.; Watkin, D. J., CRYSTALS version 12: software for guided crystal structure analysis. *Journal of Applied Crystallography* **2003,** *36* (6), 1487.
9. Palatinus, L.; Chapuis, G., SUPERFLIP - a computer program for the solution of crystal structures by charge flipping in arbitrary dimensions. *Journal of Applied Crystallography* **2007,** *40* (4), 786-790.
10. Blum, V.; Gehrke, R.; Hanke, F.; Havu, P.; Havu, V.; Ren, X.; Reuter, K.; Scheffler, M., Ab initio molecular simulations with numeric atom-centered orbitals. *Computer Physics Communications* **2009,** *180* (11), 2175-2196.
11. Bhattacharya, S.; Kanai, Y., Spin-orbit-coupling-induced band splitting in two-dimensional hybrid organic-inorganic perovskites: Importance of organic cations. *Physical Review Materials* **2023,** *7* (5), 055001.
12. Perdew, J. P.; Ernzerhof, M.; Burke, K., Rationale for mixing exact exchange with density functional approximations. *The Journal of chemical physics* **1996,** *105* (22), 9982-9985.
13. Tkatchenko, A.; DiStasio, R. A.; Car, R.; Scheffler, M., Accurate and Efficient Method for Many-Body van der Waals Interactions. *Phys. Rev. Lett.* **2012,** *108* (23), 236402.
14. Heyd, J.; Scuseria, G. E.; Ernzerhof, M., Hybrid functionals based on a screened Coulomb potential. *The Journal of chemical physics* **2003,** *118* (18), 8207-8215.
15. Huhn, W. P.; Blum, V., Benchmarking Post-SCF Treatments of Spin-Orbit Coupling in Electronic Structure Theory. In *APS March Meeting Abstracts*, 2016; Vol. 2016, p B20.003.
16. Liu, C.; Huhn, W.; Du, K.-Z.; Vazquez-Mayagoitia, A.; Dirkes, D.; You, W.; Kanai, Y.; Mitzi, D. B.; Blum, V., Tunable Semiconductors: Control over Carrier States and Excitations in Layered Hybrid Organic-Inorganic Perovskites. *Physical Review Letters* **2018,** *121* (14), 146401.
17. Togo, A.; Shinohara, K.; Tanaka, I., Spglib: a software library for crystal symmetry search. *Science and Technology of Advanced Materials: Methods* **2024,** *4* (1), 2384822.
18. Li, X.; Hoffman, J. M.; Kanatzidis, M. G., The 2D Halide Perovskite Rulebook: How the Spacer Influences Everything from the Structure to Optoelectronic Device Efficiency. *Chemical Reviews* **2021,** *121* (4), 2230-2291.
19. Lepetit, L.; Chériaux, G.; Joffre, M., Linear techniques of phase measurement by femtosecond spectral interferometry for applications in spectroscopy. *J. Opt. Soc. Am. B* **1995,** *12* (12), 2467-2474.
20. Maznev, A. A.; Nelson, K. A.; Rogers, J. A., Optical heterodyne detection of laser-induced gratings. *Opt. Lett.* **1998,** *23* (16), 1319-1321.

21. Goodno, G. D.; Miller, R. J. D. In *Ultrafast optically heterodyne detected transient grating spectroscopy using diffractive optics*, International Quantum Electronics Conference, San Francisco, California, 1998/05/03; Corkum, P.; Peyghambarian, N., Eds. Optica Publishing Group: San Francisco, California, 1998; p QWD7.
22. Goodno, G. D.; Astinov, V.; Miller, R. J. D., Diffractive Optics-Based Heterodyne-Detected Grating Spectroscopy: Application to Ultrafast Protein Dynamics. *The Journal of Physical Chemistry B* **1999,** *103* (4), 603-607.
23. Xu, Q.-H.; Ma, Y.-Z.; Fleming, G. R., Heterodyne detected transient grating spectroscopy in resonant and non-resonant systems using a simplified diffractive optics method. *Chemical Physics Letters* **2001,** *338* (4), 254-262.
24. Brixner, T.; Mancal, T.; Stiopkin, I.; Fleming, G., Phase-stabilized Two-dimensional Electronic Spectroscopy. *The Journal of chemical physics* **2004,** *121*, 4221-36.
25. Hybl, J. D.; Albrecht Ferro, A.; Jonas, D. M., Two-dimensional Fourier transform electronic spectroscopy. *The Journal of Chemical Physics* **2001,** *115* (14), 6606-6622.
26. Gan, Z.; Gloor, C. J.; Yan, L.; Zhong, X.; You, W.; Moran, A. M., Elucidating phonon dephasing mechanisms in layered perovskites with coherent Raman spectroscopies. *The Journal of Chemical Physics* **2024/08/21,** *161* (7).
27. Cowan, M. L.; Ogilvie, J. P.; Miller, R. J. D., Two-dimensional spectroscopy using diffractive optics based phased-locked photon echoes. *Chemical Physics Letters* **2004,** *386* (1), 184-189.
28. Moran, A. M.; Maddox, J. B.; Hong, J. W.; Kim, J.; Nome, R. A.; Bazan, G. C.; Mukamel, S.; Scherer, N. F., Optical coherence and theoretical study of the excitation dynamics of a highly symmetric cyclophane-linked oligophenylenevinylene dimer. *The Journal of Chemical Physics* **2006,** *124* (19), 194904.